Condensation, evaporation, melting, and crystallization in the primitive solar nebula: Experimental data in the system MgO-SiO$_2$-H$_2$ to 1.0 × 10^{-9} bar and 1870 °C with variable oxygen fugacity

Bjorn O. Mysen, Ikuo Kushiro*

Geophysical Laboratory, Carnegie Institution of Washington, 2801 Upton Street, N.W., Washington, D.C. 20008, U.S.A.

Abstract

Crystal-vapor, melt-vapor, and crystal-melt-vapor phase relations in the system MgO-SiO$_2$-H$_2$ have been determined at low pressures (10^{-4} to 10^{-9} bar) and high temperature (1400 to 1870 °C) from vapor-pressure determinations of periclase, forsterite, silica minerals, enstatite, and liquid compositions in the system and from conventional phase-equilibrium measurement techniques. In addition to pressure, temperature, and bulk-composition variables, the oxygen fugacity was varied from 1.5 orders of magnitude above that of the iron-wüstite oxygen buffer to about 2.5 orders of magnitude below.

In this system, periclase, forsterite, and silica (tridymite and cristobalite) evaporate congruently to a gas phase consisting of MgO, SiO$_2$, SiO, Si, and oxygen species, whereas enstatite (most likely protoenstatite) evaporates incongruently to forsterite plus a silica-rich vapor. Liquid is unstable at silicate vapor pressures below 10^{-5} to 10^{-6} bar. The temperatures of the triple points where crystals, liquid, and gas coexist range from 1550 °C for enstatite, to 1600 °C for silica and 1700 °C for forsterite. The temperature of the triple point for periclase was not determined, but is likely to be near 2800 °C. The pressures of the triple points increase by several orders of magnitude upon dilution of the vapor phase to hydrogen/silicate molar ratios relevant to condensation in the solar nebula (e.g., 10^4), and the temperatures decrease by several hundred degrees.

Vaporous diagrams in the systems MgO-SiO$_2$ and MgO-SiO$_2$-Fe show that at pressures and hydrogen/silicate ratios appropriate for the solar nebula, the vaporous phase is forsterite with a vaporous field extending from about 95–99 mol% MgO (forsterite-periclase vaporous boundary) to less than 10 mol%, where the enstatite and forsterite coexist. These relations are consistent with extensive Mg-Si fractionation by fractional condensation of forsterite during cooling in the early solar nebula. In the Fe-bearing, ternary system the forsterite vaporous extends to nearly 100% Fe, thus suggesting that very extensive magnesiosilicate fractional condensation (and temperature reduction—at least 400 °C) is necessary before Fe metal will condense from the early solar nebula.

Introduction

Chemical, isotopic, and petrographic evidence, in particular from carbonaceous chondrites, indicates that the formation of rock-forming minerals in the solar nebula was the result of processes that include evaporation to and condensation of liquid and crystals from a vapor phase (Grossman, 1980; Wood, 1984; Grossman and Larimer, 1974; MacPherson and Grossman, 1979; Lattimer and Grossman, 1978; Cameron and Fegley, 1982; Onuma et al., 1979; Nagahara, 1984). Both evaporation-condensation and melting-crystallization may have occurred repeatedly both locally and regionally (Herndon, 1978; Nagahara, 1981; Wood, 1984; Niederer and Papanastassiou, 1984; Chou et al., 1976; Clayton et al., 1977). The bulk compositions of individual grains and agglomerates that

accreted to form meteorite parent bodies and terrestrial planets depend critically, however, on the extent to which their early nebula-formation processes were governed by vapor-crystal equilibria or vapor-liquid-crystal equilibria and also on the extent to which these were equilibrium processes. Whether or not condensation and evaporation processes include formation of liquids depends on pressure, temperature, and bulk composition of the system (for data on commonly cited models, see for example, Cameron, 1973, 1978; Cameron and Fegley, 1982; Wood, 1981, 1984; Ahrrenius and Alfven, 1971). For a given bulk composition, there is a minimum pressure above which a crystalline phase cannot condense directly from a gas phase or evaporate directly to a gas without an intervening liquid field. Liquid, crystal(s), and gas coexist at triple points. It is important, therefore, to establish the pressure-temperature conditions of the triple point (as well as other invariant points) for relevant nebular materials.

The oxygen fugacity in the nebula most likely was governed by C-O-H gas equilibria and can be calculated as a function of gas composition and temperature. Redox equilibria involving major elements such as Fe, Si, and less abundant Ti, P, and Cr may be influenced by the oxygen fugacity in the f_{O_2} ranges suggested for the early history of the solar nebula. Moreover, the pressure-temperature-composition stability relations of oxides, metals, and silicates may be functions of the oxygen fugacity of the system. Estimates of the f_{O_2} range from about 5–6 orders of magnitude below that of the iron wüstite (IW) buffer for the nebular gas (Fegley, 1985) to 1–2 orders of magnitude above the IW buffer for "whole-rock" CAI inclusions from Allende as recorded with measurements of intrinsic oxygen fugacity (Kozul et al., 1986). Ihinger and Stolper (1986) from spectroscopic studies of hibonite from CAIs suggested f_{O_2} values during crystallization of hibonite from ~5 orders of magnitude below that of the IW buffer to values slightly above those of the magnetite-wüstite (MW) buffer.

Pressure, temperature, and oxygen-fugacity conditions during formation of the mineral assemblages in the matrix, chondrules, and inclusions in chondritic meteorites reflect conditions in the early solar nebula. This pressure, temperature, and oxygen-fugacity environment can be characterized provided that crystal-liquid, liquid-vapor, and crystal-vapor phase-equilibrium data for the relevant mineral assemblages have been experimentally obtained under realistic pressure, temperature, and bulk-composition conditions. These calculations also require knowledge of which phases were involved in the nebular condensation history. From data on free energies of formation of relevant phases, condensation sequences have been calculated (e.g., Grossman and Larimer, 1974; Lattimer and Grossman, 1978). Those calculations rely on accurate thermochemical data and on a knowledge of the speciation in the gas phase under appropriate conditions. The thermodynamic data are not always available. In particular, thermochemical data for the most refractory oxides as well as liquids are rare. Characterization of the species of the gas phase has been reported for only very limited chemical compositions and under restricted pressure, temperature, and oxygen-fugacity conditions. The types of crystalline phases included in the calculations depend on their detection in extraterrestrial materials.

Experimental determination of phase relations of individual minerals and mineral assemblages does not rely on the above information. Experimental determination of evaporation-condensation behavior in appropriate compositions has been reported only for a few systems (Sata et al., 1978; Masuda and Tanaka, 1979; Hashimoto, 1983; King, 1982; Hashimoto et al., 1979; Mysen et al., 1985) under restricted conditions. The oxygen fugacity was not a controlled variable in these studies.

In order to provide a framework for phase relations in the nebular environment, it is necessary to determine systematically the phase relations in relevant simple oxide 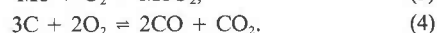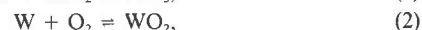and silicate systems and then proceed with more complex systems before an adequate description of phase relations among gas, liquid, and crystalline phases in the solar nebula is feasible. The system MgO-SiO_2 contains the important phases forsterite and enstatite in addition to periclase and one or more silica polymorphs (depending on the temperature range; Fenner, 1913). Characterization of the phase relations in this system will provide, for example, data relevant to understanding the systematic variations in Mg/Si among chondrites (e.g., Urey, 1961; Ahrens, 1964, 1965; Wasson, 1974) as well as differences in Mg/Si between inclusions, chondrules, and matrix within individual chondrites (Huss et al., 1981; Nagahara, 1984). The bulk Mg/Si of the terrestrial planets also differs (Weidenschilling, 1976; Turekian and Clark, 1969). There is also evidence that the Earth's upper mantle is not chondritic (Palme and Nickel, 1985). Furthermore, detailed information on phase relations along this join is necessary to develop the phase relationships in the more complex, and more realistic, systems MgO-Al_2O_3-SiO_2 and CaO-MgO-Al_2O_3-SiO_2.

EXPERIMENTAL METHODS

Starting materials were (1) finely ground (1–3 μm) synthetic forsterite crystallized at 1000 °C and 15 kbar for 24 h from a spectroscopically pure mixture of $MgO + SiO_2$ with about 5 wt% H_2O (this procedure yields 100% reaction and produces 20–50-μm euhedral forsterite crystals); (2) synthetic, spectroscopically pure tridymite for SiO_2; and (3) spectroscopically pure MgO.

All experiments were conducted in a high-temperature (~2000 °C), high-vacuum ($P \leq 10^{-11}$ bar) furnace described by Mysen et al. (1985). Briefly, the experiments were conducted in a 5.0-cm-long and 1-cm-diameter, W-wound furnace coaxially located in a cylindrical, 35-cm-long by 18-cm-diameter vacuum chamber. The temperature was measured with a W-$W_{74}Re_{26}$ thermocouple interfaced with a programmable temperature controller (Hadidiacos, 1979). The temperature, calibrated against the melting point of Pt (1772 °C) and Fe (1535 °C), is accurate to ±5 °C. The precision is better than ±2 °C. The temperature gradient along a 0.5-cm vertical zone in the furnace is less than 10 °C. The samples were contained in 2-mm-diameter (inside diameter) by 2-mm-deep Mo, W, and C containers with a 0.5-mm-thick tight-fitting lid. These containers were suspended in the furnace with a 0.25-mm-diameter wire fed through two 0.5-mm-diameter holes drilled in the side of the containers. The container was placed within 1-mm of the thermocouple junction.

The three different sample container materials were used so that the oxygen fugacity could be buffered at different values by interaction between oxygen in the sample and the metal container with the following possible reactions:

$$W + 1.5O_2 \rightleftharpoons WO_3, \tag{1}$$
$$W + O_2 \rightleftharpoons WO_2, \tag{2}$$
$$Mo + O_2 \rightleftharpoons MoO_2, \tag{3}$$
$$3C + 2O_2 \rightleftharpoons 2CO + CO_2. \tag{4}$$

The temperature trajectories of the f_{O_2} defined by these reactions are shown in Figure 1. Although it is not altogether clear whether the W-containing buffer is that described by Reaction 1 or Reaction 2 because their ΔG values are nearly identical (Robie et al., 1978), it is clear that these buffer assemblages cover an f_{O_2} range from about 1.5 order of magnitude above to about two orders of magnitude below that of the iron-wüstite buffer.

For experiments involving liquid ⇌ vapor equilibria (see also below), it was desirable to control the pressure in the vacuum chamber. Because H_2 was the principal component in the solar nebula, H_2 was used for this purpose. P_{H_2} inside the vacuum chamber (but not necessarily within the sample containers; see discussion below) were measured with a Varian Ratiomatic 842 ionization gauge. The pressure was maintained by bleeding H_2 into the vacuum chamber through a valve placed in front of one of the ports into the main vacuum chamber. The measured pressure, P_{tot}, is, therefore, equal to $P_{H_2} + P_{vac}$, where P_{vac} is the pressure in the vacuum chamber with the H_2 valve closed. In the experiments reported here, P_{vac} was 1.0×10^{-10} bar or less, so that with the P_{H_2} above 1.0×10^{-9} bar, the measured P_{tot} values are near the P_{H_2} values in the vacuum chamber. Except at $P_{H_2} \geq 1.0 \times 10^{-6}$ bar, where the P_{tot} fluctuated by as much as 2% during experiments lasting several hours (probably owing to convection inside the vacuum chamber), the P_{H_2} is precise to at least 1%.

The experiments were terminated by turning off the power to the furnace. Although the quenching rate depends on the temperature, rates near 10–20 °C/s between 1500 °C and 1000 °C were obtained. Because cooling was principally by radiative transfer, cooling to lower temperatures was significantly slower.

Chemical analysis and petrographic studies were performed with optical microscopy and with a JEOL-35 scanning-electron microscope equipped with both wavelength- and energy-dispersive detection systems for quantitative analysis. Analyses of quenched liquids were conducted with a 10 μm × 10 μm square raster, and averages of 5 to 10 such analyzed squares are reported.

The pressure inside the sample containers is not necessarily the same as in the vacuum chamber (outside the capsule). With the outside pressure significantly lower than the vapor pressure of the samples, the Knudsen method (Knudsen, 1909) can be used to determine the vapor pressure of the samples. Two 0.5-mm-diameter holes were drilled in the sides of the container walls to generate a Knudsen cell (Knudsen, 1909). Because these two holes also facilitate suspension of the containers from the sample-suspension wire inserted in the furnace, the effective orifice area, after subtraction of Mo wire cross-section, is 2.95×10^{-3} cm².

With the Knudsen method, the vapor pressure of a substance, P_m (bar), can be determined by measuring the evaporation rate, $\partial w/\partial t$ (g/s) (Paule and Margrave, 1967);

$$P_m = \frac{1}{Ac} \frac{\partial w}{\partial t} \sqrt{\frac{2\pi RT}{M}}, \qquad (5)$$

where A is the area of the orifice (cm²), c is the Clausing factor, M is the molecular weight of the effusing vapor, T is absolute temperature, and R is the gas constant.

Equation 5 is strictly valid only under the following conditions. (1) The sample surface is infinitely large compared with the orifice area. (2) The evaporation constant is unity. (3) The length of the orifice is negligible. (4) The ambient pressure is such that there is no interaction between the gas molecules ("free molecule regime"). Because these conditions cannot be strictly met experimentally, the P_m in Equation 5 is not the equilibrium vapor pressure, P_v, but can be related to P_v by the relationship (Motzfeldt, 1955)

$$P_v = \{1 + f[(1/a) + (1/W) - 2]\}P_m. \qquad (6)$$

In this equation, $f = cA/A_0$, where A_0 is the evaporation surface area, α is the evaporation constant, and W is the Clausing factor
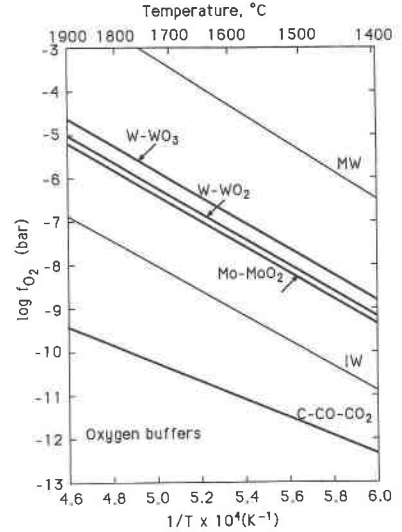
for a container with orifice and evaporation surface areas equal. In the present experiments, an empirical factor that includes the entity $\{1 + f[(1/\alpha) + (1/W) - 2]\}$ was calibrated by using known substances with well-characterized pressure versus temperature relationships. The present system was calibrated with liquid Cu and Ag (Jones et al., 1927). Results of rate studies at different temperatures and different run durations are given in Table 1. The empirical pressure-correction factor obtained from those data $(4.0 \pm 1.0 \times 10^4)$ was used to compare results for vapor pressures of SiO_2 with thermodynamic data from the literature. The experimental P_v data from SiO_2 were obtained with a range of weight losses (8.4–86%; see Table 2). Thus, despite the fact that in principle there might be a change in pressure as a function of the extent of weight loss due to the open-system nature of the present experiments, this effect is small and is neglected. With this proviso, the heat and entropy of evaporation (ΔH_v and ΔS_v, respectively) can then be related to the vapor pressure as follows:

$$\ln P_v = (-\Delta G_v/RT) = (-\Delta H_v/RT) + (\Delta S_v/R). \qquad (7)$$

Porter et al. (1955) used alumina Knudsen cells and obtained ΔH_v for SiO_2 near 570 kJ/mol. Although those experiments were reported to have been conducted under "neutral f_{O_2} conditions," possible contamination of the silica by Al_2O_3 at the high temperatures of those experiments (up to 1900 K) was not consid-

Fig. 1. Oxygen fugacity–temperature trajectories for MW (magnetite-wüstite), IW (iron-wüstite), W-WO₃, W-WO₂, Mo-MoO₂, and C-CO-CO₂ oxygen buffers. The tungsten and molybdenum buffer curves were calculated from Robie et al. (1978). Other curves are from Huebner (1971).

TABLE 1. Experimental results for Cu and Ag metal

Starting material	T (°C)	P_{H_2} (bar)	Time (min)	Phases present	Loss (mg)	Loss (wt%)
Ag	1200	1.0×10^{-9}	20	Ag(Liq)	4.60	29.3
Ag	1100	1.0×10^{-9}	120	Ag(Liq)	5.72	36.6
Cu	1327	1.0×10^{-9}	120	Cu(Liq)	3.83	43.8

Note: All sample containers were of Mo.

TABLE 2. Experimental results

Starting material	T (°C)	P_{H_2} (bar)	Time (min)	Cap-sule	Phases present	Loss (mg)	Loss (wt%)
Tr	1400	1.8×10^{-9}	3800	Mo	Tr + Qz + V	0.87	18.9
Tr	1400	1.8×10^{-8}	1600	Mo	Tr + Qz + V	0.60	11.2
Tr	1450	1.8×10^{-9}	3975	Mo	Tr + Qz + V	1.50	25.4
Tr	1450	1.8×10^{-9}	9900	Mo	Tr + Qz + V	3.76	57.7
Tr	1500	1.8×10^{-9}	360	Mo	Cr + Qz + V	0.45	8.4
Tr	1500	1.8×10^{-9}	1440	Mo	Cr + V	1.84	30.8
Tr	1500	1.8×10^{-8}	1440	Mo	Cr + V	2.12	43.2
Tr	1595	1.8×10^{-9}	400	Mo	Cr + V	1.88	37.2
Tr	1595	1.8×10^{-9}	1020	Mo	Cr + V	4.17	86.0
Tr	1618	$5.0 \times 10^{-5*}$	120	Mo	Cr + L + V	≤2.33	≤40.7
Tr	1618	1.8×10^{-4}	120	Mo	Cr + L + V	1.26	40.6
Tr	1640	$5.0 \times 10^{-5*}$	120	Mo	Cr + L + V	1.28	21.8
Tr	1640	1.8×10^{-9}	150	Mo	Cr + L + V	1.25	28.4
Tr	1640	1.8×10^{-9}	300	Mo	Cr + L + V	2.90	58.8
Tr	1661	$5.0 \times 10^{-5*}$	120	Mo	Cr + L + V	1.68	25.1
Tr	1661	1.8×10^{-4}	120	Mo	Cr + L + V	0.66	12.8
Tr	1678	1.8×10^{-4}	120	Mo	Cr + L + V	1.71	31.3
Tr	1708	1.8×10^{-9}	120	Mo	Cr + L + V	3.62	68.2
Tr	1752	1.8×10^{-9}	60	Mo	L + V	2.57	55.9
Tr	1500	1.8×10^{-8}	1080	W	Cr + V	0.56	14.0
Tr	1550	2.2×10^{-8}	2880	W	Cr + V	2.41	71.9
Tr	1600	1.8×10^{-8}	120	W	Cr + V	0.33	6.4
Tr	1400	$1.0 \times 10^{-9**}$	4080	C	Tr + V	3.89	97.3
Tr	1500	$1.0 \times 10^{-9**}$	360	C	Cr + V	4.91	92.6
Tr	1500	$1.0 \times 10^{-9**}$	240	C	Cr + V	3.90	67.9
Tr	1550	$1.0 \times 10^{-9**}$	60	C	Cr + V	1.69	45.1
Tr	1600	$1.0 \times 10^{-9**}$	20	C	Cr + V	1.83	51.0
Pe	1750	1.8×10^{-9}	120	Mo	Pe + V	2.05	91.1
Pe	1700	1.8×10^{-9}	300	Mo	Pe + V	2.02	92.7
Pe	1650	1.8×10^{-9}	4100	Mo	E	≥1.73	100.0
Pe	1650	1.8×10^{-8}	105	Mo	Pe + V	0.69	39.0
Pe	1600	1.8×10^{-8}	360	Mo	Pe + V	0.68	35.1
Pe	1550	1.8×10^{-8}	360	Mo	Pe + V	0.60	29.6
Pe	1500	1.8×10^{-9}	1385	Mo	Pe + V	1.25	64.4
Pe	1450	1.8×10^{-9}	940	Mo	Pe + V	0.60	22.7
Fo	1400	1.8×10^{-9}	14400	Mo	Fo + V	1.17	20.3
Fo	1500	1.8×10^{-9}	3970	Mo	Fo + V	1.02	15.8
Fo	1500	1.8×10^{-9}	5760	Mo	Fo + V	1.14	25.1
Fo	1500	1.8×10^{-9}	11424	Mo	Fo + V	2.85	56.2
Fo	1595	1.8×10^{-9}	720	Mo	Fo + V	1.16	22.5
Fo	1595	1.8×10^{-9}	1440	Mo	Fo + V	2.05	34.5
Fo	1680	1.8×10^{-9}	180	Mo	Fo + V	2.28	41.2
Fo	1680	1.8×10^{-9}	300	Mo	Fo + V	3.32	63.4
Fo	1680	1.8×10^{-9}	870	Mo	E	n.r.	100.0
Fo	1702	1.8×10^{-7}	30	Mo	Fo + L (q-Fo) + V	1.16	17.5
Fo	1702	1.8×10^{-4}	20	Mo	Fo + L (q-Fo) + V	0.43	8.9
Fo	1724	1.8×10^{-4}	15	Mo	Fo + L (q-Fo) + V	0.23	4.8
Fo	1724	1.8×10^{-7}	15	Mo	Fo + L (q-Fo) + V	1.29	20.3
Fo	1746	1.8×10^{-7}	15	Mo	Fo + L (q-Fo) + V	2.85	57.8
Fo	1769	1.8×10^{-9}	30	Mo	E	n.r.	100.0
Fo	1769	1.8×10^{-9}	15	Mo	E	n.r.	100.0
Fo	1769	1.8×10^{-7}	1	Mo	Fo + L (q-Fo) + V	1.27	25.5
Fo	1769	1.8×10^{-7}	5	Mo	Fo + L (q-Fo) + V	4.30	76.1
Fo	1769	1.8×10^{-7}	15	Mo	E	n.r.	100.0
Fo	1769	1.8×10^{-4}	5	Mo	Fo + L (q-Fo) + V	0.17	3.5
Fo	1869	1.8×10^{-4}	5	Mo	L (q-Fo) + V	2.06	50.5
Fo	1700	1.8×10^{-4}	30	Mo	Fo + L (q-Fo) + V	0.80	17.7
Fo	1600	1.8×10^{-8}	900	W	Fo + V	1.93	42.2
Fo	1675	1.8×10^{-8}	120	W	Fo + V	2.92	78.1
Fo	1600	$1.0 \times 10^{-9**}$	330	C	Fo + V	1.14†	34.4
Fo	1540	$1.0 \times 10^{-9*}$	850	C	Fo + V	0.44	11.3
Fo	1600	$1.0 \times 10^{-9*}$	260	C	Fo + V	1.47	27.5
Fo	1650	$1.0 \times 10^{-9*}$	180	C	Fo + V	1.10	33.6

Note: Tr = tridymite; Cr = cristobalite; Qz = quartz; Fo = forsterite; Pe = periclase; L = liquid; V = vapor; q-Fo = quench forsterite; n.d. = not determined; n.r. = not resolved; E = capsule empty after experiment.
* Ar used as pressure medium. ** No H. † Incomplete sample recovery.

ered. Hidalgo (1960) reported this relationship between temperature and vapor pressure:

$$\ln P_v = (-57\,800/T) + 18.4, \qquad (8)$$

which is shown as the line marked "H" in Figure 2. T is absolute temperature. As can be seen from those data, there is agreement between the two data sets. All calculations of equilibrium vapor pressure from the observed weight-loss data were, therefore, conducted with Equation 5 with an empirical correction factor obtained from the weight-loss data for liquid Cu and Ag.
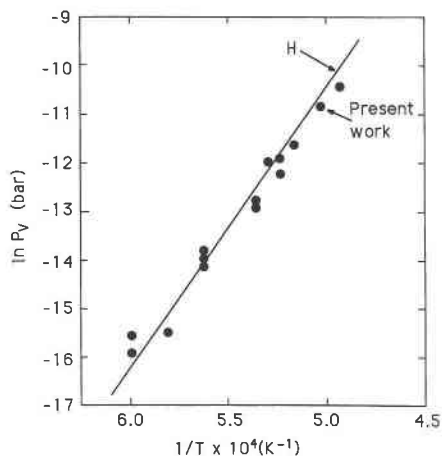
Fig. 2. Observed vapor pressure (P_v) of silica as a function of temperature. Curve H is from Hidalgo (1960).

RESULTS

The system SiO₂-H₂

Experiments in the system SiO₂-H₂ were conducted in the P_{H_2} range between 1.8×10^{-4} and 1.8×10^{-9} bar and in the T range between 1400 and 1752 °C with all experimental data shown in Table 2. Most of the experiments were carried out in Mo containers with the f_{O_2} buffered along the Mo-MoO₂ curve (Fig. 1). In all subsolidus experiments, 10–30-μm euhedral cristobalite and tridymite crystals were formed. At the lowest temperatures, quartz is also present (Table 2). Most likely, the quartz was formed during the relatively slow quenching. The observed vapor pressures in the subsolidus region (Fig. 3) were fitted to a linear expression of the form of equation (7),

$$\ln P_v = [(-58\,307 \pm 5152)/T] + 18.6 \pm 3.0, \quad (9)$$

where T is absolute temperature. The data are insufficiently precise to discriminate between evaporation of tridymite and cristobalite. The experimental data with W containers (Fig. 3) showed significantly more scatter and can be described with the expression

$$\ln P_v = [(-57\,546 \pm 14\,803)/T] + 17.3 \pm 8.2. \quad (10)$$

The two curves cannot be separated within experimental uncertainty.

There is a distinct difference in slope and intercept for the vapor-pressure curves obtained with experiments in graphite capsules (C-CO-CO₂-O₂ oxygen buffer) (Fig. 3), as expressed numerically with the expression

$$\ln P_v = [(-68\,826 \pm 4871)/T] + 27.0 \pm 2.8, \quad (11)$$

compared with the results obtained with Mo and W sample containers. This significantly steeper slope and larger value at the intercept is a function of the 2.5–3.5 orders of magnitude decrease in f_{O_2} resulting from using graphite rather than Mo or W containers.
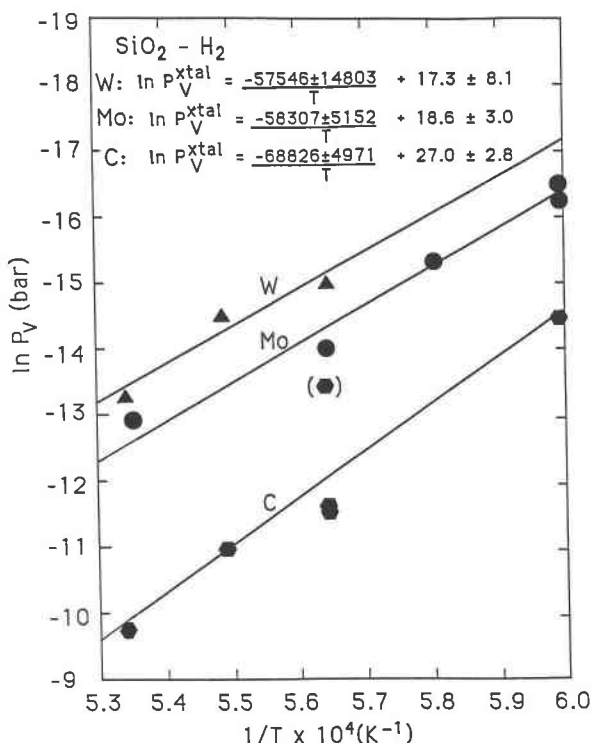

Fig. 3. Observed vapor pressure of crystalline silica (cristobalite and tridymite) with different container materials as indicated. The point in parentheses is most probably inaccurate because of partial blockage of the holes in the W container in that experiment.

Liquid, which quenches to a clear, bubble-free glass, was found to coexist with euhedral 10–30-μm cristobalite at temperatures above 1600 °C, and only liquid (glass) exists in experiments at temperatures above 1700 °C (Fig. 4). This observation contrasts with that for phase relations in the SiO₂ system at 1 bar, where cristobalite melts congruently at 1713 °C (Fenner, 1913). This melting interval, therefore, (1) either results from chemical impurity (contamination), (2) a ~100 °C temperature gradient vertically along 3 mm in the furnace, (3) or the phase relations cannot be described simply in terms of the unary system SiO₂. A solidus depression resulting from H₂ solution in the melt is ruled out as unlikely in view of the fact that this depression requires about 25 mol% H₂ in solution.

Although not detected experimentally, the topology of the phase relations depicted in Figure 4 requires that there should be a phase field between Cr + L + V and V involving vapor and another phase, possibly a liquid of different composition than the liquid coexisting with vapor at temperatures above about 1700 °C.

Electron-microprobe analyses of quenched glasses and coexisting cristobalite show at most 0.4 wt% Al₂O₃ in the quenched glass (Table 3), possibly resulting from vapor transport of Al₂O₃ from the alumina furnace tube. One-bar liquidus phase relations on the join SiO₂-Al₂O₃ (Ara-
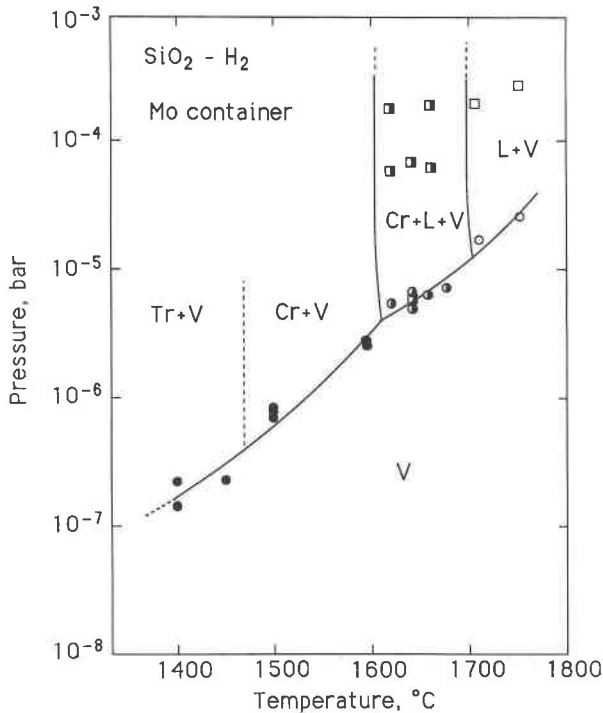
Fig. 4. Pressure-temperature phase relations in the system SiO₂-H₂ at the oxygen fugacity of the Mo-MoO₂ buffer. The pressure axis is total pressure (silicate vapor pressure + hydrogen pressure). In experiments along the vaporous, the silicate vapor pressure is approximately equal to total pressure because P_{H_2} is one or more order of magnitude less than the silicate vapor pressure. Closed symbols, no liquid present; half-open symbols, liquid and crystals present; open symbols, liquid and no crystals present. Circles denote experiments used for vapor-pressure determination. Squares represent experiments at imposed pressures greater that vapor pressure. Note that although there must be an additional phase field between the Cr + L + V and V fields, this is not indicated because of lack of experimental information.

maki and Roy, 1959) indicate, however, that about 5 wt% Al₂O₃ is required for a 100 °C liquidus temperature depression along the join at 1 bar. There is no other chemical contamination of the system, and this expla-
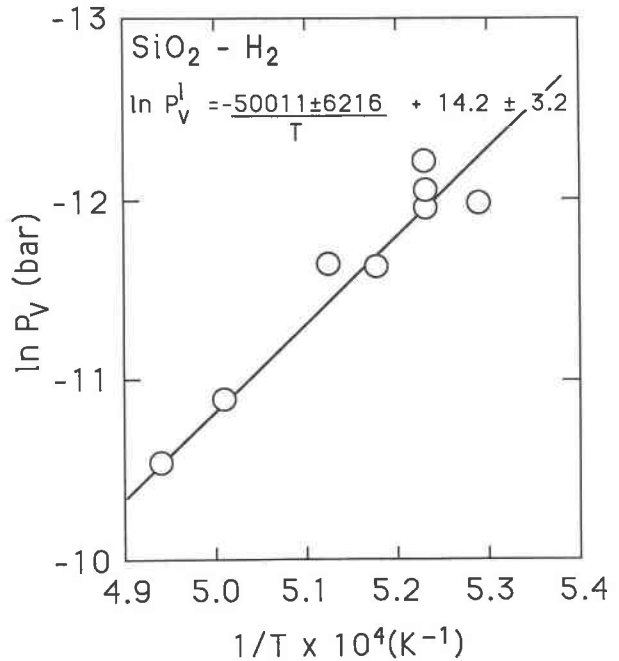

Fig. 5. Vapor pressure of molten silica (P_v) as a function of temperature with Mo sample containers.

nation is ruled out to explain the existence of a melting interval below the 1-bar liquidus of SiO₂. As indicated above, the temperature gradient along a 3-mm section of the furnaces is less than 10 °C, and explanation 2, requiring a ~100 °C gradient is, therefore, implausible. It appears, therefore, that the only viable explanation for the temperature depression of the solidus and the existence of a melting interval is that the melt is partially dissociated into SiO₂, SiO (and possibly Si), and oxygen, where oxygen may combine with ambient H₂ to form water. Sosman (1965) suggested that addition of 5 wt% Si to SiO₂ might result in a ≥100 °C liquidus depression on this join, which is in general accord with results of preliminary experiments on this join shown in Table 4.

The suggested partial dissociation of SiO₂ in the melt is also consistent with the magnitude of the change in slope of the vaporous curves when liquid appears on the vaporous (Fig. 4). Least-squares regression of the vapor-pressure data for liquid SiO₂ (Fig. 5) obtained with Mo containers results in the expression

$$\ln P_v = (-50011 \pm 6216/T) + 14.2 \pm 3.2. \quad (12)$$

TABLE 3. Chemical compositions, SiO₂ system

	$P_{H_2} = 1.8 \times 10^{-4}$ bar, $T = 1670$ °C		$P_{H_2} = 1.8 \times 10^{-4}$ bar, $T = 1650$ °C	
	Cristobalite	Glass	Cristobalite	Glass
Si	47.51	46.83	47.13	47.35
Al	0.20	0.16	0.16	0.18
Mg	0.01	0.00	0.00	0.00
O	53.74	53.03	53.19	53.33
Total	101.16	100.03	100.73	100.86
Atomic proportions (O = 2)				
Si	1.006	1.006	1.013	1.013
Al	0.006	0.006	0.006	0.006
Mg	0.000	0.000	0.000	0.000
O	2.000	2.000	2.000	2.000

TABLE 4. Preliminary results, SiO₂-Si system

Run no.	Starting material	T (°C)	P (bar)	Time (min)	Phases present†
2882*	1Si·3SiO₂	1624	1.0×10^{-8}	240	Cr + 2 liquids
2883*	1Si·9SiO₂	1624	1.0×10^{-8}	90	Cr + liquid
2892**	1Si·9SiO₂	1602	9.0×10^{-8}	240	Cr + SiO
2894**	1Si·9SiO₂	1669	9.0×10^{-8}	90	Cr + liquid

* Sealed Pt containers. ** Mo Knudsen cells with H₂ as pressure medium.
† Cr = cristobalite.
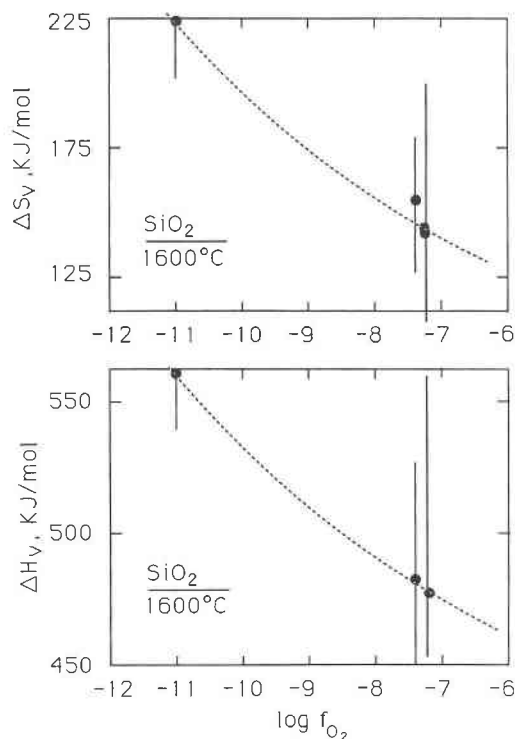
Fig. 6.   Enthalpy and entropy of vaporization (ΔH_v and ΔS_v, respectively) of silica at 1600 °C as a function of oxygen fugacity (f_{O_2}).
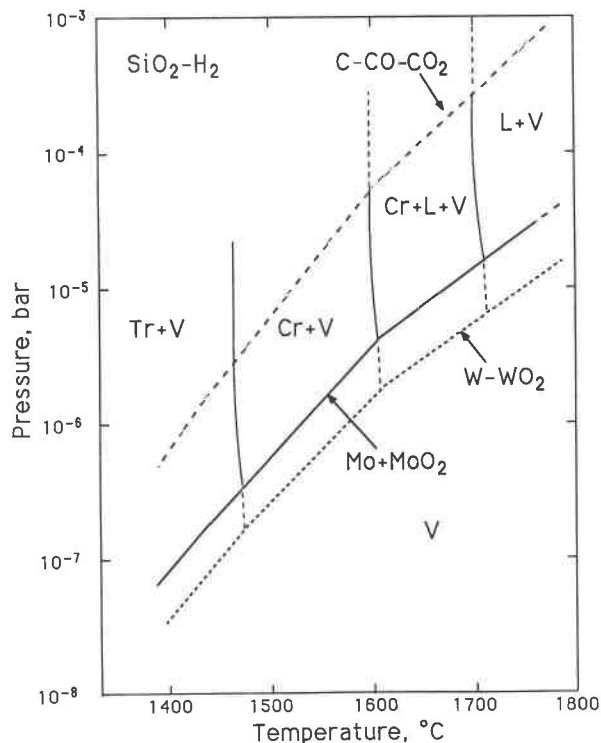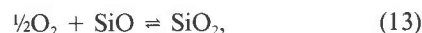

Fig. 7.   Pressure-temperature phase relations in the system SiO$_2$-H$_2$ at different oxygen fugacities (as indicated on the figure). The pressure axis is total pressure (silicate vapor pressure + hydrogen pressure). In experiments along the vaporous, the silicate vapor pressure is approximately equal to total pressure because P_{H_2} is one or more orders of magnitude less than the silicate vapor pressure. Note that although there must be an additional phase field between the Cr + L + V and V fields, this is not indicated because of lack of experimental information.

The ambient P_{H_2} in the experiments used to obtain the coefficients in Equation 12 ranged from 1.8×10^{-8} to 1.8×10^{-4} bar. In this P_{H_2} range, no effect of the ambient pressure on the observed vapor pressures was observed.

The enthalpies and entropies of vaporization, derived from the data in Figure 3, are shown in Table 5. The differences between ΔH_v and ΔS_v for the Cr $\rightleftharpoons$ V and the L $\rightleftharpoons$ V curves, are the enthalpies and entropies associated with the melting and other possible processes such as partial dissociation of SiO$_2$ in the liquid, for example (see also below for further discussion of this possibility). Both values [~72 kJ/mol and ~37 J/(mol·K)] are significantly greater than the enthalpy and entropy of fusion of cristobalite at 1 bar [8.9 kJ/mol and 4.5 J/(mol·K), respec-

TABLE 5.   Thermochemical data

Material	Reaction*	Container	ΔH_v (kJ/mol)	ΔS_v [J/(K·mol)]
SiO$_2$	X,V	W	478 ± 123	143 ± 68
SiO$_2$	X,V	Mo	484 ± 43	155 ± 25
SiO$_2$	X,V	C	572 ± 41	224 ± 23
SiO$_2$	L,V	Mo	416 ± 52	118 ± 26
Mg$_2$SiO$_4$	X,V	C	667 ± 206	241 ± 110
Mg$_2$SiO$_4$	X,V	Mo	640 ± 36	210 ± 54
Mg$_2$SiO$_4$	L,V	Mo	550 ± 110	179 ± 54
MgO	X,V	Mo	321 ± 32	63 ± 17

* Reaction X,V denotes evaporation of crystalline material. Reaction L,V denotes evaporation of liquid.

tively; Richet and Bottinga, 1986]. The ΔH and ΔS of the reaction (Robie et al., 1978)

$$\tfrac{1}{2}O_2 + SiO \rightleftharpoons SiO_2, \tag{13}$$

are about -780 kJ/mol and 244 J/(mol·K), respectively. Although the thermodynamic data for Equation 13 are for crystalline materials, it would seem that partial dissociation of SiO$_2$ in the liquid would more readily account for the difference between ΔH and ΔS from Equations 9 and 12 than simply those associated with melting.

The use of graphite capsules rather than Mo or W results in a lowering of the f_{O_2} of between three and four orders of magnitude. This f_{O_2} reduction results in the 19% increase in the slope of the vapor-pressure curve and also a change in the intercept (Fig. 3; see also Eqs. 9–11). This change in slope, expressed in terms of ΔH_v and ΔS_v (Fig. 6), results in a significant increase in both enthalpy and entropy [from 480 to 570 kJ/mol and 155 to 224 J/(mol·K), respectively]. These increases are consistent with increased degree of dissociation of SiO$_2^{gas}$ to SiO^{gas} + O$_2^{gas}$. From the thermodynamic data of Stull and Prophet (1971), complete dissociation of SiO$_2^{gas}$ would result in a 110 kJ/
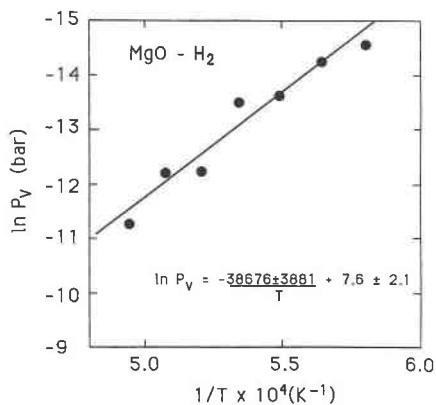
Fig. 8.   Vapor pressure (P_v) of crystalline MgO (periclase) as a function of temperature (Mo sample containers).

mol increase in ΔH_v. Within the uncertainty of the data reported here, the calculated change is similar to the observed value. It appears, therefore, that the reduction of f_{O_2} from that of Mo-MoO$_2$ (or the less accurate tungsten–tungsten oxide buffer) to that of the C-CO-CO$_2$ buffer may have resulted in substantial, perhaps complete, dissociation of SiO$_2^{gas}$ to SiO^{gas} + O$_2^{gas}$. Further dissociation to elemental Si is likely only if a significant proportion of the gas species formed in equilibrium with the Mo-MoO$_2$ oxygen buffer include SiO and O$_2$.

From the thermodynamic data summarized in Table 5, a phase diagram for SiO$_2$ as a function of pressure, temperature, and oxygen fugacity is suggested (Fig. 7). In constructing this diagram, it was assumed that the ΔH and ΔS of melting derived from the results with the Mo-MoO$_2$ buffer are not significantly affected by the lowering of f_{O_2} to that of the C-CO-CO$_2$ buffer. The reduction of the oxygen fugacity has a very substantial influence on the minimum pressure below which liquid cannot exist in this system (about 2.5 orders of magnitude). This difference is a consequence of the partial (or complete?) reduction of SiO$_2$ in the gas to SiO and O$_2$ and perhaps even Si.

The system MgO-H$_2$

The vapor pressures above crystalline MgO under appropriate temperature–oxygen fugacity conditions are needed in order fully to characterize the phase relations on the join MgO-SiO$_2$ even though periclase itself may not have been an important phase in the petrogenetic history of the early solar nebula.

Because the oxygen fugacities necessary to dissociate MgO to Mg and O$_2$ (Lou et al., 1985) are far below those attainable with the experimental design used here, the vapor pressures above MgO were determined only with Mo containers (Fig. 8; see also Table 2). Furthermore, this f_{O_2} is so low that equilibria involving oxygen and metallic Mg are not relevant to petrogenetic processes in the early solar nebula.
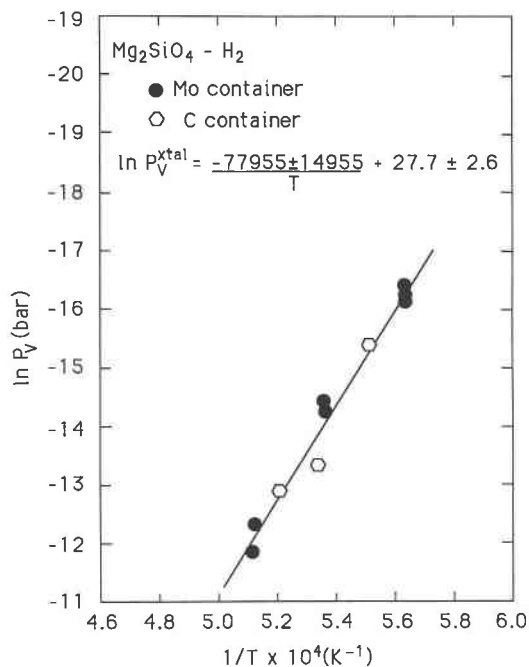

Fig. 9.   Vapor pressure of crystalline forsterite (P_v) as a function of temperature with Mo (filled circles) and C (open hexagons) containers.

The vapor-pressure data were fitted to a straight line,

$$\ln P_v = (-38\,676 \pm 3881/T) + 7.6 \pm 2.1, \quad (14)$$

with the derived enthalpy, entropy, and free energy of evaporation shown in Table 5. The free energy of evaporation from Equation 14 at 1900 K, for example, is 202 kJ/mol as compared with 250 kJ/mol as calculated from the JANAF tables (Stull and Prophet, 1971). The ΔG_v for the reaction

$$\text{MgO}^{xtal} = \text{Mg}^{gas} + \text{O}_2^{gas} \quad (15)$$
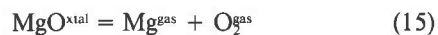
at the same temperature is 774 kJ/mol. This much higher value thus lends further support to a suggestion that in these experiments, most likely periclase evaporates to MgO gas.

The system Mg$_2$SiO$_4$-H$_2$

Evaporation behavior and phase relations in the system Mg$_2$SiO$_4$-H$_2$ are shown in Figures 9–11 with experimental results in Table 2. Sata et al. (1978) suggested that forsterite might evaporate incongruently to periclase + vapor. Despite extensive search and very long experimental run duration (Table 2), no evidence for the proposed incongruency was found. The forsterite is pure or nearly pure (Table 6) Mg$_2$SiO$_4$ with no evidence of significant contamination from the furnace (Al from the furnace tube or Mo from the sample container) as would be expected because of the many orders of magnitude lower vapor pressures of Mo and Al (or Al$_2$O$_3$) (e.g., Jones et al., 1927; Stull and Prophet, 1971) compared with those of forsterite.
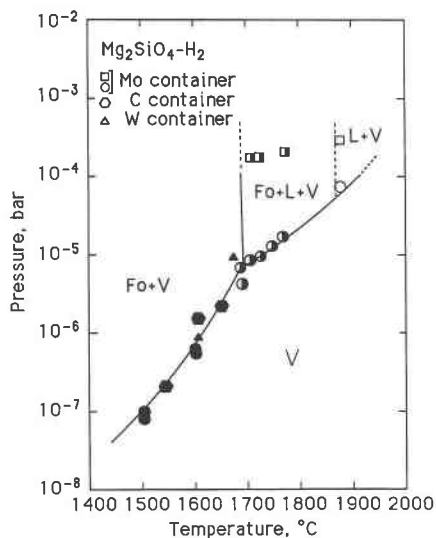
Fig. 10. Pressure-temperature phase relations in the system Mg$_2$SiO$_4$-H$_2$ at different oxygen fugacities (as indicated by different symbols in the figure). The pressure axis is total pressure (silicate vapor pressure + hydrogen pressure). In experiments along the vaporous, the silicate vapor pressure is approximately equal to total pressure because P_{H_2} is one or more orders of magnitude less than the silicate vapor pressure. Closed symbols, no liquid present; half-open symbols, liquid and crystals present; open symbols, liquid and no crystals present. Note that although there must be an additional phase field between the Fo + L + V and V fields, this is not indicated because of lack of experimental information.

The vapor pressure above crystalline forsterite was determined as a function of temperature in Mo and C containers (Fig. 9), but within experimental uncertainty (5–10%), no effect of different container material could be discerned. Linear regression of all the data points results in the expression

$$\ln P_v = (-77\,955 \pm 4955/T) + 27.7 \pm 2.6, \quad (16)$$

with the entropy and enthalpy of evaporation derived from Equation 16 in Table 5. The absence of discernible f_{O_2}-dependence differs from the behavior of pure SiO$_2$ (Fig. 3), where a 19% increase in the ΔH_v was observed. This difference in behavior most likely results from the fact that the mole fraction of SiO$_2$ in the Mg$_2$SiO$_4$ system is 0.333. Because only the SiO$_2$ component in the gas phase undergoes reduction with decreasing f_{O_2}, resulting in a 19% increase in the slope of the SiO$_2$ evaporation curve, only about a 6% effect would be expected in the Mg$_2$SiO$_4$ system. A 6% change in slope and intercept is within the uncertainty of the Mg$_2$SiO$_4$ vapor-pressure data in Figure 9.

Small amounts of interstitial melt were detected at temperatures near 1700 °C (Fig. 10). The liquid does not quench to glass, but exists as fibrous, quench forsterite along grain boundaries to temperatures near 1870 °C, where the experimental charges consist of all quench ol-

TABLE 6.   Chemical compositions, forsterite

P_{H_2} (bar):	1.8×10^{-9}	1.8×10^{-7}	1.8×10^{-7}
T (°C):	1500	1769	1746
SiO$_2$	41.56	41.74	42.81
Al$_2$O$_3$	0.58	0.94	0.84
MgO	58.48	57.94	57.96
Total	100.62	100.62	101.61
Atomic proportions (O = 4)			
Si	0.969	0.973	0.988
Al	0.016	0.027	0.023
Mg	2.035	2.016	1.992

ivine (Table 2). The temperature of the onset of melting is 170–190 °C below the suggested liquidus temperature of forsterite at 1 bar (1890 ± 20 °C; Bowen and Andersen, 1913; Bowen and Schairer, 1936) where forsterite melts congruently. The 1870 °C phase boundary between forsterite + liquid + vapor and liquid + vapor (Fig. 10) accords, within experimental error, with the suggested 1-bar liquidus temperature for forsterite (note, however, that the 1-bar liquidus temperature of forsterite is an extrapolated value from data along the joins Mg$_2$SiO$_4$-Fe$_2$SiO$_4$ and Mg$_2$SiO$_4$-SiO$_2$).

The phase relations in the system Mg$_2$SiO$_4$-H$_2$ (Fig. 10) are topologically similar to those of the system SiO$_2$-H$_2$, in which case there is a melting interval between 1600 and 1700 °C where cristobalite coexists with liquid and vapor. As for the silica system there is no evidence of contamination and thermal gradients within the furnace, and it is suggested, therefore, that the melting interval is the result of partial dissociation of silica in the liquid and the system is MgO-SiO$_2$-SiO-O$_2$ rather than Mg$_2$SiO$_4$. It should also be noted that the topology of the diagram in Figure 10 also requires an additional phase field between that of forsterite + liquid + vapor and that of vapor only. This field has not been detected experimentally, however, and is not included in the figure.

Two vapor pressure–temperature curves in the temperature range of liquid have been determined (Fig. 11). There is a steep curve that is defined by the weight-loss data at an imposed P_{H_2} of 1.8×10^{-8} bar,

$$\ln P_v = [(-185\,390 \pm 14\,365)/T] + 82.7 \pm 7.2, \quad (17)$$

and there is a curve with a much less steep slope at $P_{H_2} = 1.8 \times 10^{-4}$ bar,

$$\ln P_v = [(-66\,173 \pm 13\,342)/T] + 21.5 \pm 6.6. \quad (18)$$

The curve defined by Equation 17 corresponds to $\Delta H_v = 1540$ kJ/mol and $\Delta S_v = 687$ J/(mol·K). This curve is physically implausible because it implies that the heat of evaporation of Mg$_2$SiO$_4$ liquid is 2.4 times greater—not less—than that of crystalline forsterite at the same temperature. This behavior may be related to the fact that the ambient pressure used during acquisition of the data behind Equation 17 is significantly less than the vapor pressure itself. Melt near forsterite composition is very
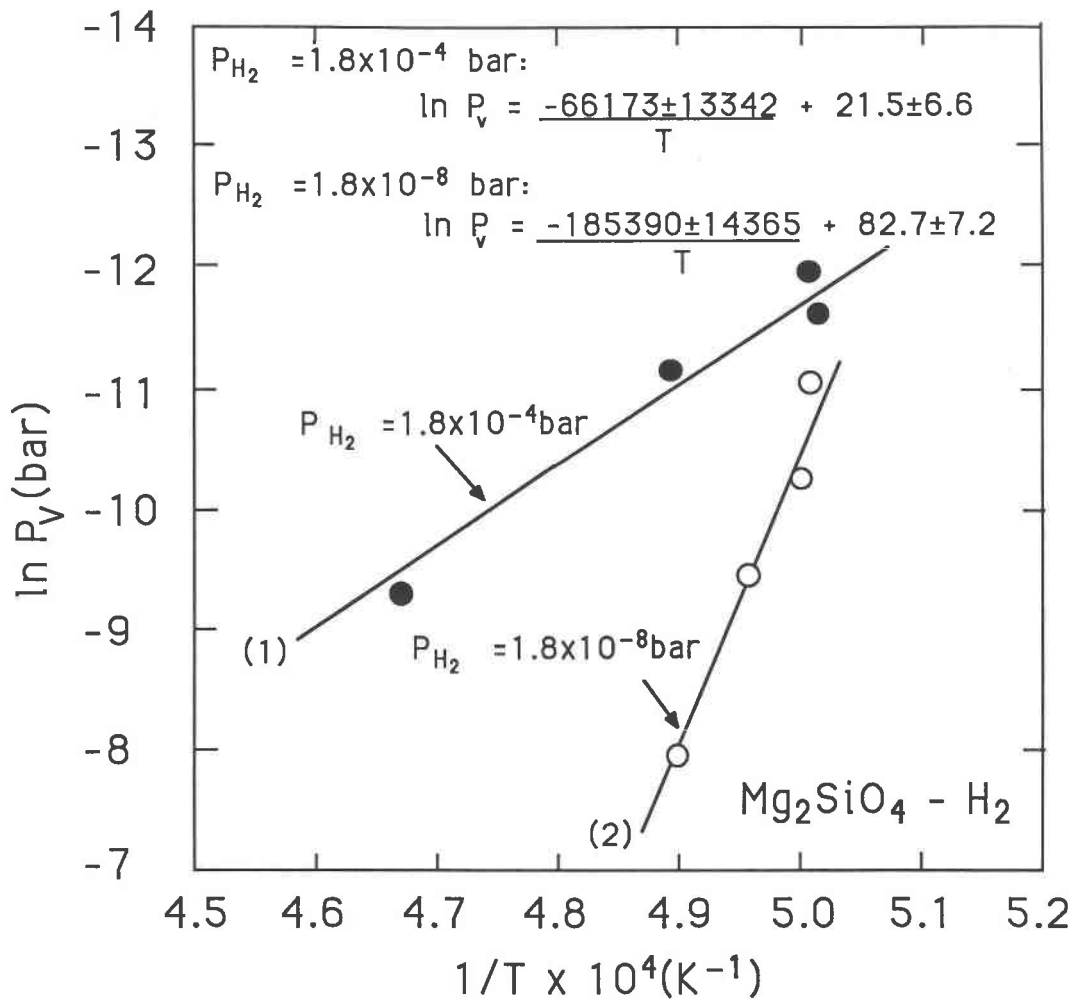
Fig. 11. Vapor pressure curves in the temperature regime of liquid present in the Mg_2SiO_4 system at two different P_{H_2} values as indicated. Note that whereas curve 1 was obtained with $P_{H_2} > P_v$, curve 2 was determined with $P_{H_2} < P_v$. See text for detailed discussion of the relationships. All experiments were conducted with Mo containers.

fluid (on the order of 1 poise or less at these temperatures). This environment is, therefore, conducive to boiling, in which case the weight-loss determinations can be too high by several orders of magnitude (Centolanzi and Chapman, 1966). This phenomenon may explain the implausibly high values of the coefficients in Equation 17.

The other curve in Figure 11 (Eq. 18) results in slightly smaller values of ΔH_v and ΔS_v than for crystalline forsterite [640 and 550 kJ/mol and 210 and 179 J/(mol·K), respectively]. The latter two sets of data correspond to ΔH_m and ΔS_m of 90 kJ/mol and 31 J/(mol·K), respectively, at the temperature of onset of melting (1700 °C). Values for enthalpy of fusion of forsterite have been suggested in the range 71 to 235 kJ/mol (Stull and Prophet, 1971; Bottinga and Richet, 1978) with most values near the lower end of this range. The value derived from the vaporization curve defined by Equation 18 also falls in the lower part of this range. This curve is, therefore, consistent with available thermodynamic data.

Discussion

Isothermal and isobaric sections

From data presented above as well as data for the join $MgSiO_3$-H_2 (Kushiro and Mysen, 1987), partly schematic, isobaric, isothermal sections in the system MgO-SiO₂-H₂ have been constructed (Figs. 12, 13). As discussed above, neither the liquid nor the vapor compositions may be described within this system, and in the absence of all but qualitative inferences on this subject, these considerations are left out. The portions of the system where this situation may affect the topology of the sections are dashed in Figure 13.

The molar ratios of hydrogen to oxide corresponding to some of the phase changes are shown as X_{H_2}/X_{MgO}, etc. Those ratios were calculated from the thermodynamic data summarized in Table 5 under the assumption that the gas phase can be treated as an ideal gas. None of the
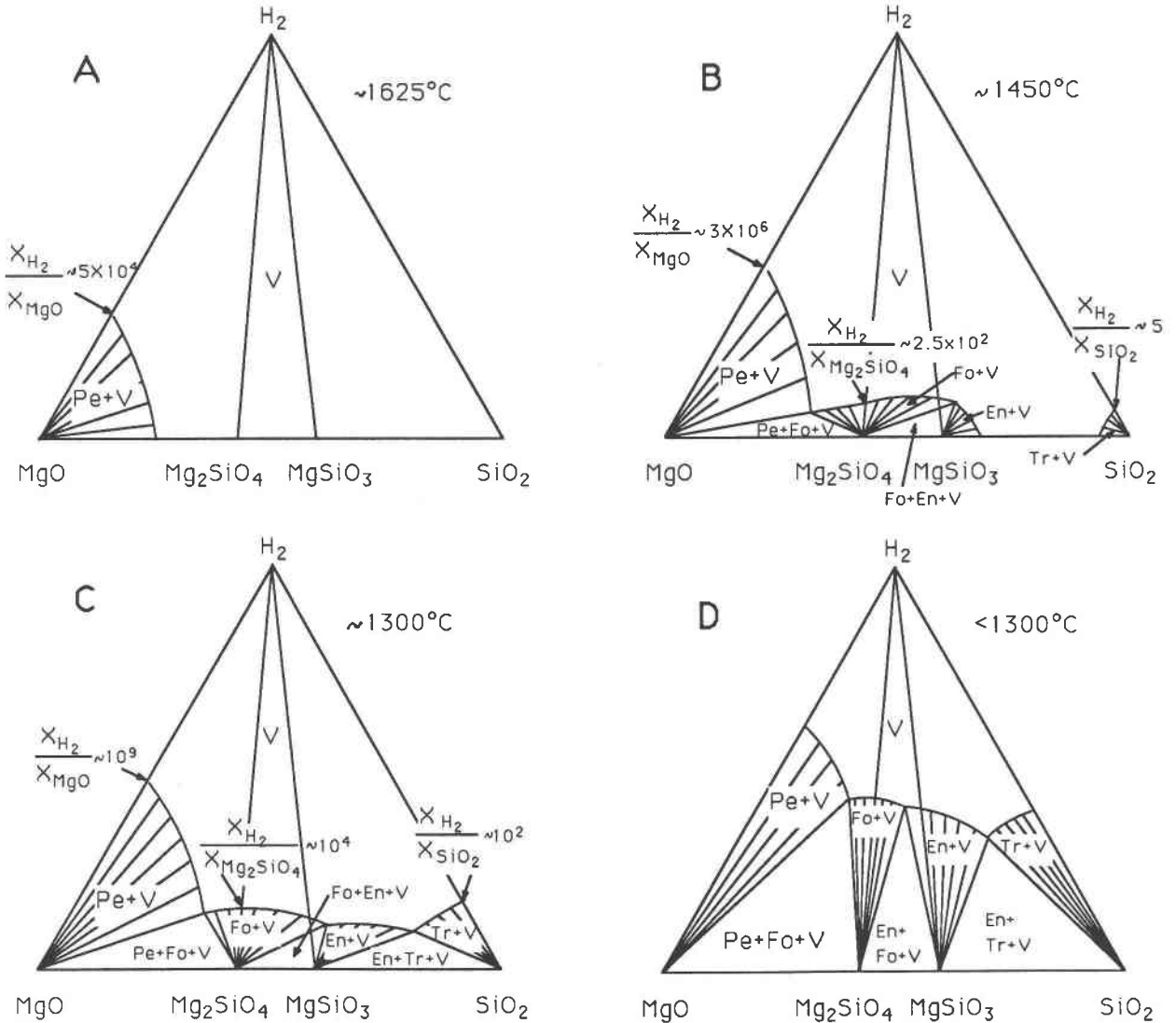
Fig. 12. Isobaric (1.0×10^{-6} bar), isothermal (1625, 1450, 1300, and <1300 °C), partially schematic sections of the system MgO-SiO₂-H₂. Note that the individual joins are not to scale in order better to illustrate the relationships. The ratios X_{H_2}/X_{MgO}, etc., represent the moles ratios of hydrogen to oxide indicated in the vapor at the intersection of a particular join and a vaporous curve.

joins are drawn to scale in order to better show the relations.

At a total pressure of 1.0×10^{-6} bar, liquid is not stable in the system MgO-SiO₂ and periclase is the first phase to condense for compositions from MgO to somewhere between MgO and Mg₂SiO₄. The exact value of $X_{MgO}/X_{Mg_2SiO_4}$ is not known. For all phase fields, the hydrogen/oxide ratio governs the phase relations at constant temperature and pressure. For periclase, forsterite, and silica

compositions, the only phase fields in question are those of oxide + vapor and vapor because these phases evaporate congruently. In those cases, evaporation can be accomplished isothermally and isobarically by increasing the hydrogen/oxide ratio. The behavior of these phases contrasts, however, with enstatite, which evaporates incongruently (Sata et al., 1978; Kushiro and Mysen, 1987; see also discussion below). At 1450 °C, for example (Fig. 12B), in the absence of H₂, enstatite (or clinoenstatite) is

P=10^{-3} bar
Weight percent
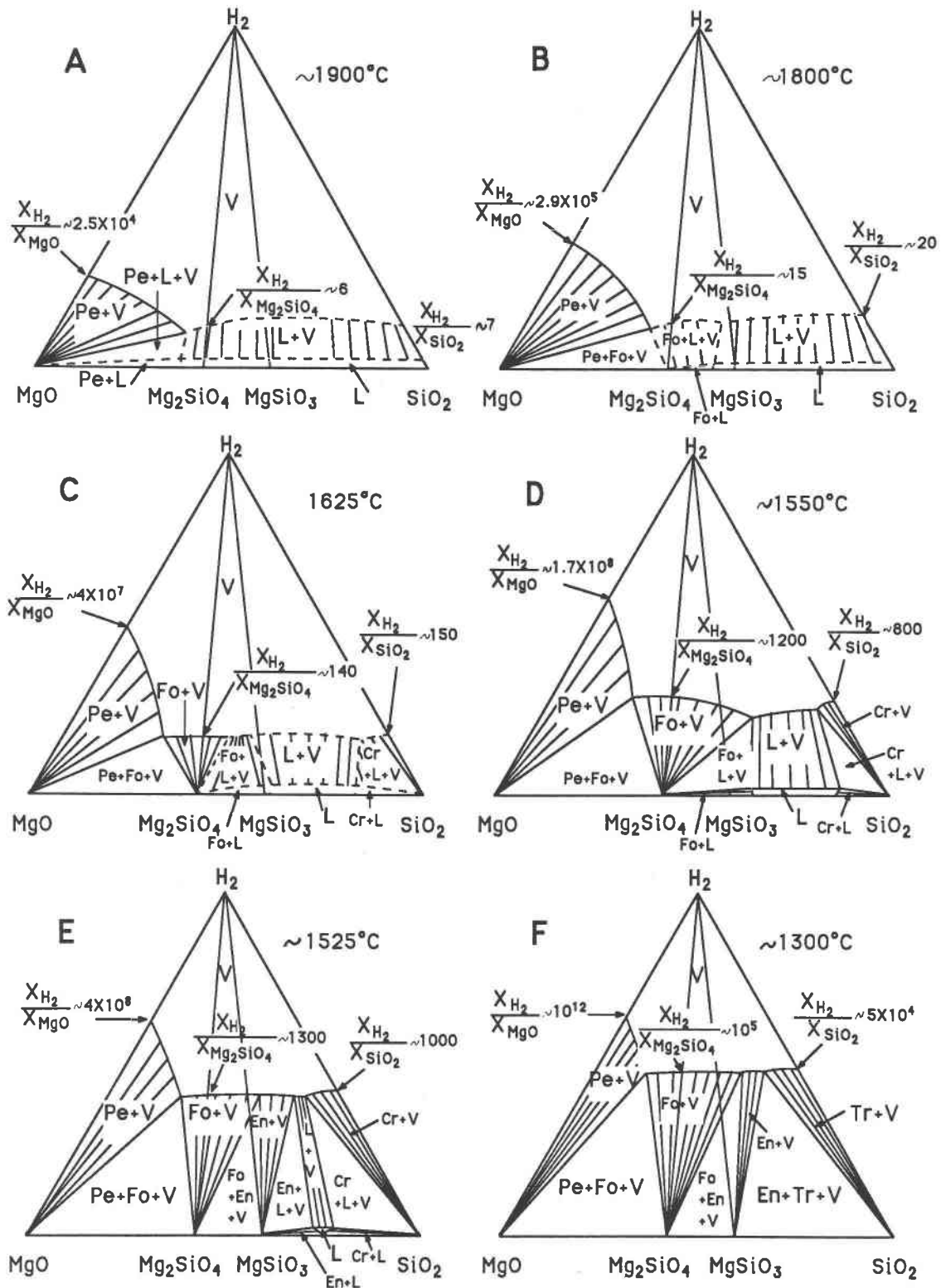
stable. Increasing $X_{H_2}/X_{silicate}$ results in the appearance first of forsterite followed by the disappearance of enstatite and, finally, the disappearance of forsterite as well.

The phase relations at a total pressure of 1.0×10^{-3} bar (Fig. 13) are more complex because liquid is also stable. Because the liquids may be partially dissociated into reduced silicon oxide components, the liquid-present fields in Figure 13 are dashed. These dashed tie lines are meant for illustrative purposes only. In this figure, the narrow field near the MgO-SiO₂ join is marked "Liquid." This field is included because some H₂ dissolves in the liquid (see also Luth and Boettcher, 1986; Luth et al., 1987, for discussion of H₂ solubility behavior in silicate melts), thus resulting in a vapor-absent field.

In the absence of H₂, vapor along all but the MgO-H₂ join will condense to liquid prior to crystallization at 10^{-3} bar. Increasing hydrogen/oxide results, however, in shrinkage of the liquid fields and their eventual disappearance. This feature is further illustrated in Figure 14, showing the minimum pressure below which liquid is not stable in the systems SiO₂-H₂ (A) and Mg₂SiO₄-H₂ (B). Silica data from both Mo-MoO₂ and C-CO-CO₂ are shown (Fig. 14A), illustrating that decreasing oxygen fugacity results in shrinking pressure-temperature stability of liquid silica.

The data in Figure 13 also show that increasing hydrogen/oxide ratio in some cases can result in solidification of liquid (Fig. 13D). At temperatures near 1550 °C, for a range of compositions between Mg₂SiO₄ and Mg/Si slightly greater than 1 (MgSiO₃ composition), either forsterite + liquid or liquid only (depending on the Mg/Si) are stable. By diluting the vapor with H₂, forsterite and vapor will be stabilized together with the liquid. The width of this field ranges to $X_{H_2}/X_{silicate}$ near 1000 for the most siliceous compositions. As even more H₂ is added to the system, the liquid will solidify with the formation of forsterite coexisting with a more magnesian vapor than that coexisting with both liquid and forsterite.

Isobaric, polythermal sections

From the ΔH_v data derived from the vapor-pressure curves in Figures 3 and 9 combined with similar data for MgSiO₃ bulk composition by Kushiro and Mysen (1987), the vaporous phase relations on the join Mg₂SiO₄-SiO₂ can be calculated as a function of temperature, oxygen fugacity, and hydrogen/silicate ratio (Fig. 15). Because of the uncertainty regarding the possible dissociation of silica in the vapor phase, the compositions are not strictly on the join Mg₂SiO₄-SiO₂, but the diagrams accurately depict the relationships of the silicate phases.

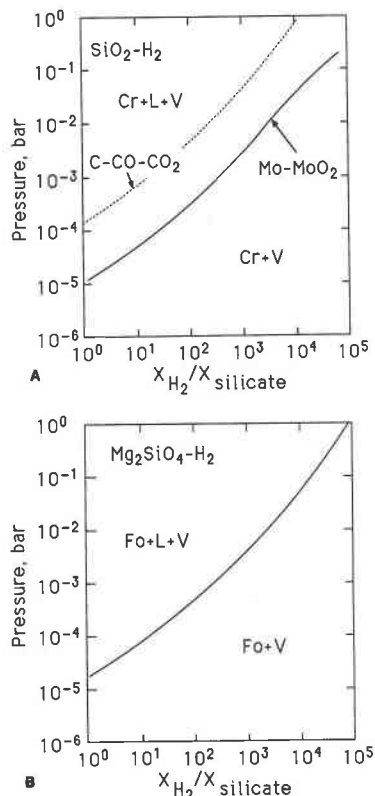Fig. 14. Minimum pressure of liquid stability as a function of mole fraction of H₂ in the gas phase for SiO₂ (A) at oxygen fugacities indicated and for Mg₂SiO₄ (B).

The diagrams (Fig. 15) were constructed as follows. The temperatures of the vaporous of the end-member compositions are from the experimental data. The topology of the phase boundaries between forsterite + vapor and vapor and between silica + vapor and vapor is calculated from the Van't Hoff equation,

$$T_E = 1/[(1/T_0) - (R \ln X_i/\Delta H_v)], \qquad (19)$$

where T_E is the temperature (K) of the vaporous at mole fraction X_i of component i, T_0 is the vaporous temperature of the pure phase, R is the gas constant, and ΔH_v is the heat of evaporation. Equation 19 is a simplification as it does not take into account dissociation in the vapor phase. The principal consequence for the vaporous diagrams of this simplification is that the forsterite vaporous surfaces will exhibit slightly less curvature in temperature-composition space than would otherwise be the case.

The join Mg₂SiO₄-SiO₂ includes enstatite, which has

←

Fig. 13. Isobaric (1.0×10^{-3} bar), isothermal (1900, 1800, 1625, 1550, 1525, and 1300 °C), partially schematic sections of the system MgO-SiO₂-H₂. Note that the individual joins are not to scale in order better to illustrate the relationships. The ratios X_{H_2}/X_{MgO}, etc., represent the molar ratios of hydrogen to oxide indicated in the vapor at the intersection of a particular join and a vaporous curve. Dashed phase fields represent compositions where most likely the composition of the liquid phase is not within the ternary system.
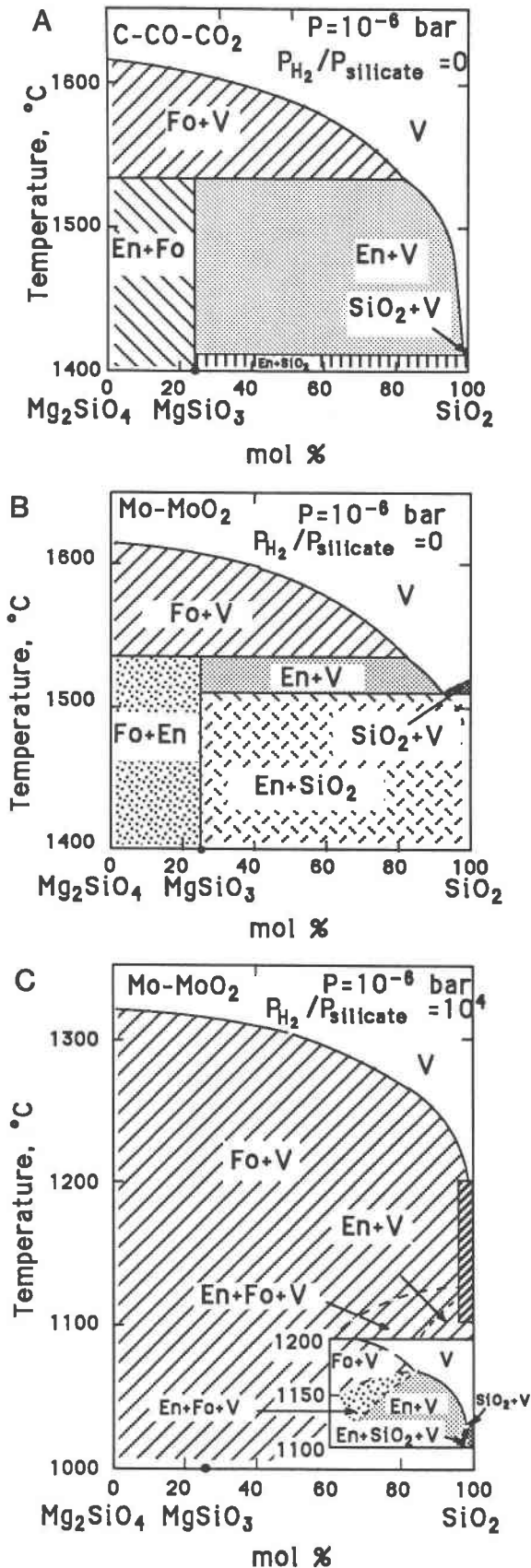
been shown to evaporate incongruently to forsterite + silica-rich vapor (Kushiro and Mysen, 1987) along a line defined by the expression

$$\ln P_v = [(-68\,908 \pm 8773)/T] + 24.3 \pm 5.0. \quad (20)$$

There is, thus, a compositional range along the join where clinoenstatite (or possibly protoenstatite) is the vaporous phase. Note, however, that because of uncertainty in structural characterization of the MgSiO$_3$ phase, this phase is simply referred to as enstatite (En). The compositional range extends from the intersection of the univariant equilibrium clinoenstatite $\rightleftharpoons$ forsterite + vapor with the forsterite vaporous to the intersection with the silica vaporous (Fig. 15). The slope of this vaporous is calculated from Equation 19 with the ΔH_v value (572 kJ/mol) from the least-square-fitted expression (Eq. 20) (Kushiro and Mysen, 1987).

As can be seen in Figure 15, forsterite is the dominant vaporous phase in the system Mg$_2$SiO$_4$-SiO$_2$ under all conditions investigated. Clinoenstatite appears on the vaporous near 82 mol% SiO$_2$, with a clinoenstatite-cristobalite eutectic at about 93 mol% SiO$_2$ at 1508 °C. The vaporous surfaces of the individual phases in this system are distinct, but different functions of $P_{H_2}/P_{silicate}$ in the gas phase:

$$T = \Delta H_v / \{\Delta S_v - [R \ln(P_{tot}/(1 + X_{H_2}))]\}, \quad (21)$$

where X_{H_2} is the $P_{H_2}/P_{silicate}$ and P_{tot} is the total pressure. With $X_{H_2} = 10^4$ (Fig. 15C), the forsterite vaporous temperature is lowered by about 300 °C, the forsterite-enstatite peritectic by about 340 °C, the silica vaporous by about 390 °C (where tridymite is now the vaporous phase), and the tridymite-enstatite eutectic by about 390 °C compared with the H$_2$-free vaporous surfaces. Notably, the temperature range over which both forsterite and enstatite occur on the vaporous is wider with the diluted gas phase than in the absence of H$_2$.

As discussed above, an effect of f_{O_2} on the slope of the vaporous could be discerned, within experimental uncertainty, for pure SiO$_2$ (Fig. 3 and 9). Thus, at given pressure, both the vaporous temperature and the heat of evaporation of SiO$_2$ (regardless of whether this is cristobalite, tridymite, or liquid) are affected. The influence of these changes on the vaporous relations along the join Mg$_2$SiO$_4$-SiO$_2$ is illustrated in Figures 15A and 15B for a total pressure of 1.0×10^{-6} bar. At this pressure, the most dramatic effect of reduction of f_{O_2} (by about 3 log units) is in the vaporous temperature (see also Figs. 3 and

---
$\leftarrow$

Fig. 15. Temperature-composition relations along the join Mg$_2$SiO$_4$-SiO$_2$ at total pressure = 1.0×10^{-6} bar in a H$_2$-free atmosphere at the f_{O_2} of the C-CO-CO$_2$ buffer (A), and at the f_{O_2} of the Mo-MoO$_2$ buffer (B), both in a H$_2$-free atmosphere, and at the f_{O_2} of the Mo-MoO$_2$ buffer with hydrogen/silicate = 10^4 (C). The hachured area in Figure 15C is presented in the insert to show detail.

9). As a result, the SiO$_2$ phase is tridymite (rather than cristobalite), and the compositional width of the tridymite vaporous is less than 1 mol% with an enstatite-tridymite eutectic temperature near 1410 °C and f_{O_2} at the C-CO-CO$_2$ buffer compared with the cristobalite-enstatite eutectic near 1510 °C and f_{O_2} at the Mo-MoO$_2$ buffer. As a result of this temperature depression, the enstatite vaporous surface is significantly wider (82–99 mol% SiO$_2$ for the f_{O_2} of the C-CO-CO$_2$ oxygen buffer and 82–94 mol% SiO$_2$ for the f_{O_2} of the Mo-MoO$_2$ oxygen buffer), and the temperature range over which enstatite will condense from a gas phase has increased from about 20 °C at the highest f_{O_2} (Mo-MoO$_2$; see Fig. 1) to about 110 °C at the lowest f_{O_2} (C-CO-CO$_2$; see Fig. 1).

On the Mg$_2$SiO$_4$-MgO join, the phase relations are controlled by a simple eutectic between periclase and forsterite because both phases evaporate congruently. The position of this eutectic is, however, quite sensitive to total pressure and dilution of the gas phase because of the large difference in ΔH_v for the two phases (see Table 5). These effects are illustrated in Figure 16. Increasing $P_{H_2}/P_{silicate}$ results in very rapid expansion of the forsterite vaporous field at the expense of periclase (Fig. 16A). Conversely, with constant $P_{H_2}/P_{silicate}$ or with no H$_2$ present at all (Fig. 16B), a very strong pressure effect is observed as decreasing pressure results in rapid expansion of the forsterite vaporous field. As a result of these two effects, the eutectic between forsterite and periclase with $P_{H_2}/P_{silicate}$ appropriate for the solar nebula (e.g., 10^4), the mole percent MgO at the eutectic is very low (0.19 mol% at $P_{tot} = 1.0 \times 10^{-4}$ bar, 1.9 mol% at 1.0×10^{-3} bar, and 7.9 mol% at 1.0×10^{-2} bar).

APPLICATIONS

Stability of liquid silicate

Determination of the pressure-temperature-composition trajectories of liquid silicates in the solar nebula is important because crystal-liquid equilibria will result in different chemical trends compared with vapor-crystal equilibria. Textural evidence from chondrules and also some inclusions in chondritic meteorites point to the existence of liquid at some stage(s) during the time of formation of these materials (e.g., Wood, 1963; Wasson, 1972; Grossman, 1980; Dodd, 1981; Nagahara, 1981).

In the Mg$_2$SiO$_4$ system (Fig. 14), liquid is stable to 1.0×10^{-5} bar at 1700 °C. Below 1.0×10^{-5} bar, crystalline forsterite will condense directly from a gas of forsterite composition. In a more realistic environment with Mg/Si = 1 (MgSiO$_3$), liquid is stable to lower pressures (2.0×10^{-6} bar) at about 1550 °C (Kushiro and Mysen, 1987). Mysen et al. (1985) found that for CaMgSi$_2$O$_6$ composition, liquid will condense from the vapor down to pressures near 3×10^{-7} bar at 1385 °C. Important ferromagnesian minerals would not condense directly from an early solar-nebula gas that contained only metal + oxygen components (no dilution of the gas phase with H$_2$, for example). Liquid would form first, and the crystalline materials would form upon cooling of this liquid.
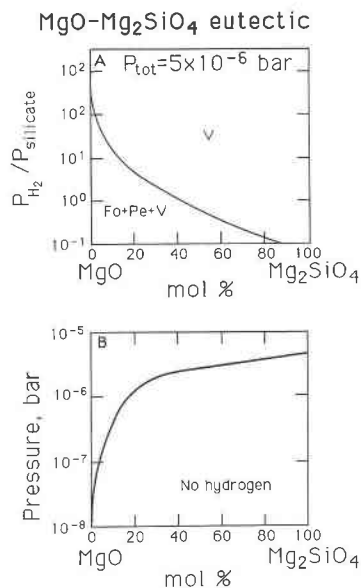

MgO-Mg$_2$SiO$_4$ eutectic

Fig. 16. The composition of the periclase-forsterite eutectic on the join MgO-Mg$_2$SiO$_4$ as a function of hydrogen/silicate ratio (A) at 5×10^{-6} bar total pressure and as a function of total pressure in a H$_2$-free atmosphere (B).

The nebular gas most likely had, however, $P_{H_2}/P_{oxide+metal}$ near 10^4. The total pressure below which liquid is not stable increases rapidly as the gas phase is diluted by H$_2$ so that at 1.0×10^4 bars, the triple point is near 2×10^{-2} bar for enstatite composition (Kushiro and Mysen, 1987). For SiO$_2$, the pressure of the triple point depends on f_{O_2} (Fig. 14A) and occurs between 1.0×10^{-1} and 1.0×10^{-2} bar. As discussed above, this oxygen-fugacity effect diminishes in importance with decreasing SiO$_2$ content of a system. The pressure of the triple point in the Mg$_2$SiO$_4$-H$_2$ system is about 5.0×10^{-2} bar (Fig. 14B) and is insensitive to f_{O_2} within the experimental uncertainty. From the experimental data of Mysen et al. (1985), the triple point for diopside composition with $P_{H_2}/P_{CaMgSi_2O_6} = 10^4$ is about 2.0×10^{-2} bar, thus resembling the pressure for MgSiO$_3$ composition. The textural evidence for liquid having existed during formation of at least portions of chondritic meteorites requires, therefore, that under equilibrium conditions, pressures must have been equal to or greater than 10^{-2} to 10^{-1} bar. Alternatively, melting may not have been an equilibrium process. Blander and Katz (1967) suggested that metastable liquid could form directly from a gas below the solidus and vaporous of minerals. Mysen et al. (1985) and Kushiro and Mysen (1987) in their melting and evaporation experiments in the systems CaMgSi$_2$O$_6$-H$_2$ and MgSiO$_3$-H$_2$, respectively, noted that liquid apparently formed almost instantly at pressure and temperature conditions corresponding to the vapor regions for those compositions. This liquid evaporated quite rapidly under such conditions. For CaMgSi$_2$O$_6$ compositions, evaporation rates in the vapor stability field were on the order of 10^{-3}
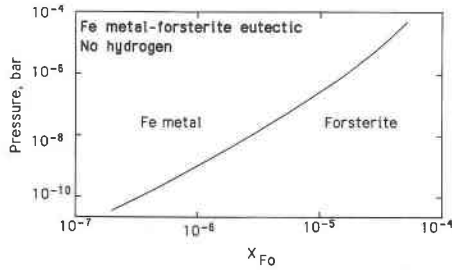
Fig. 17. Mole fraction of Mg_2SiO_4 component (X_{Fo}) of the forsterite–Fe metal eutectic on the join Fe-Mg_2SiO_4 as a function of total pressure in the absence of H_2. Thermodynamic data for Fe from Stull and Prophet (1971).

Fig. 18. Calculated phase relations near silicate–Fe metal vaporous boundaries that total pressure of 1.0×10^{-4} bar with hydrogen/silicate ratio at 10^4. The paired numbers, 2.9×10^{-9}/ 912 °C etc., represent mole fraction of forsterite in the gas relative to Fe at a particular invariant point and the temperature of this point. Note that the joins are not drawn to scale for clarity although the relative positions of points (S, a–e) are correct.

$g/(s \cdot cm^2)$ in the vapor stability field, whereas the evaporation rates at similar temperatures but at pressures where liquid or crystalline diopside was stable, the rates were on the order of 10^{-8} g/(sec·cm²). Similar observations were made for the $MgSiO_3$-H_2 system. Quenched glasses obtained from experiments of 1 to 2 min in the pressure range 10^{-9} to 10^{-8} bar showed extensive textural evidence of bubble formation. Melting of precursor materials by, for example, lightning or impact (see, for example, Wood, 1967; Nagahara, 1981) could, therefore, occur at pressures and temperatures well within the vapor stability field of the materials. In order to preserve the liquid, these melts could only have experienced these temperature conditions for periods on the order of minutes. This order of magnitude for the time of melting accords with experimental results on Na evaporation from chondrule-like spheres by Tsuchiyama et al. (1981).

Fractional condensation and chemical trends in the solar nebula

The range in compositions where forsterite is a vaporous phase in the MgO-SiO₂ system was quantified in Figure 15. Those results indicate that forsterite is the vaporous phase over the entire range of Mg/Si suggested for the solar system from the composition of carbonaceous chondrites (e.g., Larimer and Anders, 1970; Wasson, 1974; Van Schmus and Wood, 1967; Mason, 1976), regardless of total pressure and hydrogen/(oxide + metal).

In view of the fact that the solar Mg/Si is near 1 and the forsterite Mg/Si is 2, condensation of forsterite shifts the Mg/Si of the residual gas phase to values less than 1. The Mg/Si of carbonaceous chondrites ranges from 1.04 to 0.93. Limited forsterite fractionational condensation or, perhaps, simple equilibrium forsterite condensation may have resulted in this variation in Mg/Si. Enstatite chondrites have Mg/Si averaging near 0.78 (e.g., Wasson, 1974). This lower Mg/Si ratio is consistent with a process of formation that involves significantly more pervasive fractional or equilibrium condensation of forsterite compared with that required to explain the variations in Mg/Si in carbonaceous chondrites. In these proposed processes of chondrite formation, fractional condensation would fractionate the Mg/Si of the residual gas more ef-
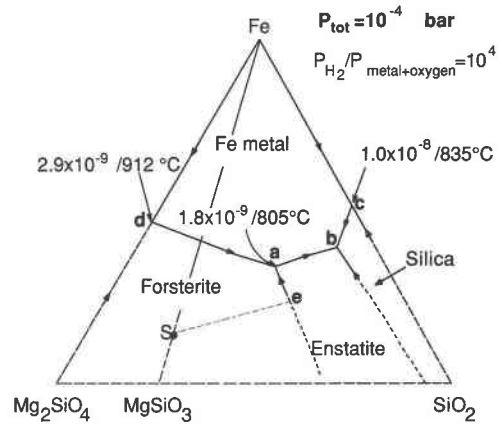
ficiently than equilibrium condensation, as will be discussed further below. Fractional evaporation is a less likely mechanism to explain this trend as this would require that the starting material (the most primitive composition) has the lowest Mg/Si and that this Mg/Si is less than the solar abundance.

The experimental data reported here may be combined with available thermodynamic data for Fe metal (Stull and Prophet, 1971) to place constraints on the relative stabilities of metallic Fe, silica, enstatite, and forsterite during condensation in the solar nebula. The composition of the forsterite–metallic Fe eutectic in the f_{O_2} range of metallic Fe stability is shown as a function of pressure in Figure 17. Those results indicate that regardless of total pressure [calculations with variable hydrogen/(oxide + silicate) will not affect these relations substantially], Fe/ Mg_2SiO_4 ratios in the gas in the range 10^5 to 10^7 are required for Fe to condense before forsterite in a H_2-free environment.

Some of the principles involved in these condensation processes are illustrated in the partially schematic vaporous diagram in Figure 18. This diagram illustrates the overall vaporous topology in the system Mg_2SiO_4-SiO_2- Fe under most realistic pressure conditions and provides some specific data for $P_{tot} = 1.0 \times 10^{-4}$ bar with $P_{H_2}/ P_{metal+oxygen} = 10^4$. Because of the extreme compositional variations in the system, the geometric representation in Figure 18 is not correct. However, the mole fractions of silicate components and temperatures of the points d and c ($X_{Mg_2SiO_4} = 2.9 \times 10^{-9}$ at 912 °C, and $X_{SiO_2} = 1.0 \times 10^{-8}$ at 835 °C) as well as of the reaction point, a ($X_{MgSiO_3} = 1.8 \times 10^{-9}$ at 805 °C), stem from the present experimental results. In terms of realistic positioning of a and b relative to Mg_2SiO_4 and SiO_2 corners, the mole fraction

of Mg$_2$SiO$_4$ component relative to SiO$_2$ component at *a* is about 90 mol% and at *b* more than 99 mol%.

Figure 18 can be used to illustrate some of the consequences of fractional and equilibrium condensation. The bulk compositions of all chondritic meteorites fall within the forsterite vaporous field with carbonaceous chondrites near or slightly to the left of the MgSiO$_3$-Fe join and enstatite chondrites significantly to the right. The solar abundance (Mg/Si = 1.06) plots slightly to the left of the join.

As in crystallization in analogous silicate melt–mineral systems, the position of the starting compositions relative to enstatite is important for the phase assemblages and compositions of the final product. For example, a bulk composition *S* will begin to condense forsterite, and as a result the vapor composition shifts toward the forsterite-enstatite vaporous boundary (intersection illustrated as *e* in Figure 18. In reality, the location of *e* is on the intersection between a line from the Mg$_2$SiO$_4$ corner through *S* and the forsterite-enstatite vaporous boundary). Further cooling of the system results in coprecipitation of forsterite and enstatite until the vapor reaches point *a* where Fe metal begins to precipitate and forsterite reacts with the vapor to produce enstatite. For starting composition *S* on the MgSiO$_3$-Fe join, the final phases will be enstatite and Fe metal. With Mg/Si of the starting composition greater than 1 (to the left of the MgSiO$_3$-Fe join), some forsterite will be left in the assemblage after final crystallization with a final phase assemblage of forsterite + enstatite + metallic Fe. With Mg/Si < 1.0, all forsterite will be consumed at *a,* and further cooling shifts the vapor composition along the Fe metal–enstatite vaporous boundary and may finally reach the eutectic, *b,* where enstatite + silica + Fe metal will condense and only H$_2$ is left in the gas phase.

The vaporous relations in Figure 18 lead to the suggestion that under equilibrium condensation conditions, compositions such as those represented by carbonaceous chondrites or the solar abundance can change only to point *a*. There is extensive evidence among unequilibrated chondrites, however, that the re-equilibration during cooling was not complete. Mg- and Fe-rich olivines coexist, sometimes in near contact, in the fine-grained matrix and where there are substantial compositional differences between the fine-grained matrix and the chondrules (e.g., Huss et al., 1981; Grossman and Wasson, 1982; Nagahara, 1981). The matrix is often very substantially enriched in Fe and Si over the chondrules and is also richer than the bulk chondrite in these components. These observations may be explained with the aid of the vaporous diagram (Fig. 18) by invoking fractional condensation (either partial or complete). Under such conditions, the condensed phase (or phases) does not re-equilibrate with the gas, and the composition of the gas phase may exhibit more extreme compositional change. If, for example, the forsterite and enstatite that crystallized between *S* and *a* in Figure 18 did not re-equilibrate with the gas phase, further cooling of a gas that has reached

point *a* from *S* by fractional condensation will move to the eutectic at point *b* where enstatite, silica, and metallic Fe will crystallize at the eutectic temperature (<800 °C) until there is only H$_2$ left in the gas phase.

It is suggested that the compositional variability exhibited both within a single chondritic meteorite as well as between different meteorite groups (e.g., carbonaceous chondrite, enstatite chondrite, and so forth) may reflect condensation from the early nebular gas with variable, but incomplete degrees of re-equilibration during condensation. Chondrule materials may represent the early stages of this processes (e.g., between *S* and a point between *e* and *a* in the schematic representation in Fig. 18). Chondrules also show evidence of melting that perhaps occurred under nonequilibrium conditions (e.g., Wood, 1967; Nagahara, 1981), thus further complicating characterization of the petrogenetic history of these materials. The dark, fine-grained, silica- and Fe-rich matrix may represent late condensates represented by condensation along the Fe metal–enstatite vaporous boundary and at the Fe metal–enstatite–silica eutectic.

REFERENCES CITED

Ahrens, L.H. (1964) Si-Mg fractionation in chondrites. Geochimica et Cosmochimica Acta, 28, 411–423.
——— (1965) Observations in the Fe-Si-Mg relationships in chondrites. Geochimica et Cosmochimica Acta, 29, 801–806.
Ahrrenius, G., and Alfven, H. (1971) Fractionation and condensation in space. Earth and Planetary Science Letters, 10, 253–267.
Aramaki, S., and Roy, R. (1959) The mullite-corundum boundary in the systems MgO-Al$_2$O$_3$-SiO$_2$ and CaO-Al$_2$O$_3$-SiO$_2$. American Ceramic Society Journal, 42, 644–645.
Blander, M., and Katz, J.L. (1967) Condensation of primordial dust. Geochimica et Cosmochimica Acta, 31, 1025–1034.
Bottinga, Y., and Richet, P. (1978) Thermodynamics of liquid silicates. Earth and Planetary Science Letters, 40, 382–400.
Bowen, N.L. (1928) The evolution of the igneous rocks, 332 p. Princeton University Press, Princeton, New Jersey.
Bowen, N.L., and Andersen, O. (1913) The binary system MgO-SiO$_2$. American Journal of Science, 37, 487–500.
Bowen, N.L., and Schairer, J.F. (1936) The system MgO-FeO-SiO$_2$. American Journal of Science, 29, 151–217.
Cameron, A.G.W. (1973) Accumulation processes in the primitive solar nebula. Icarus, 18, 407–540.
——— (1978) Physics of the primitive solar accretion disk. Moon and Planets, 18, 5–40.
Cameron, A.G.W., and Fegley, M.B. (1982) Nucleation and condensation in the primitive solar nebula. Icarus, 52, 1–13.
Centolanzi, F.J., and Chapman, D.R. (1966) Vapor pressure of tektite glass and its bearing on tektite trajectories determined from aerodynamic analysis. Journal of Geophysical Research, 71, 1735–1749.
Chou, C.L., Baedecker, P.A., and Wasson, J.T. (1976) Allende inlcusions: Volatile-element distribution and evidence for incomplete volatilization of presolar solids. Geochimica et Cosmochimica Acta, 40, 85–94.
Clayton, R.N., Onuma, N., Grossman, L., and Maeda, T.K. (1977) Distribution of the presolar component in Allende and other carbonaceous chondrites. Earth and Planetary Science Letters, 34, 209–224.
Dodd, G.R. (1981) Meteorites: A petrological-chemical synthesis, 368 p. Cambridge University Press, Cambridge.
Fegley, M.B. (1982) Hibonite condensation in the solar nebula. Lunar and Planetary Science, Proceedings, 13, 211–212.

———(1985) Oxidation state indicators of the solar nebula. Lunar and Planetary Science, Proceedings, 16, 232–233.

Fenner, C.N. (1913) The stability of the silica minerals. American Journal of Science, 36, 331–384.

Grossman, L. (1980) Refractory inclusions in the Allende meteorite. Annual Review of the Earth and Planetary Sciences, 8, 559–609.

Grossman, L., and Larimer, J.W. (1974) Early chemical history of the solar system. Reviews of Geophysics and Space Physics, 12, 71–103.

Grossman, J.N., and Wasson, J.T. (1982) Evidence for primitive nebular components in chondrules from the Chainpur chondrite. Geochimica et Cosmochimica Acta, 46, 1081–1099.

Hadidiacos, G.C. (1979) Quench furnace controller. Carnegie Institution of Washington Year Book 78, 679–682.

Hashimoto, A. (1983) Evaporation metamorphism in the early solar nebula—Evaporation experiments on the melt FeO-MgO-SiO$_2$-CaO-Al$_2$O$_3$ and chemical fractionations of primitive materials. Geochemical Journal, 17, 111–145.

Hashimoto, A., Kumazawa, M., and Onuma, N. (1979) Evaporation metamorphism of primitive dust in early solar nebula. Earth and Planetary Science Letters, 43, 13–21.

Herndon, J.M. (1978) Re-evaporation of condensed matter during the formation of the solar system. Transactions of the Royal Society of London, 363, 283–288.

Hidalgo, H. (1960) Ablation of glassy materials around blunt bodies of revolution. American Rocket Society Journal, 30, 806–814.

Huebner, J.S. (1971) Buffering techniques for hydrostatic systems at elevated pressures. In G.C. Ulmer, Ed., Research techniques for high pressure and high temperature, p. 123–178. Springer-Verlag, New York.

Huss, G.R., Keil, K., and Taylor, G.J. (1981) The matrices of unequilibrated chondrites: Implications for the origin and history of chondrites. Geochimica et Cosmochimica Acta, 45, 33–51.

Ihinger, P.D., and Stolper, E. (1986) The color of meteoritic hibonite: An indicator of oxygen fugacity. Earth and Planetary Science Letters, 78, 67–80.

Jones, H.A., Langmuir, I., and Mackay, G.M.J. (1927) The rates of evaporation and the vapor pressures of tungsten, molybdenum, platinum, nickel, iron, copper and silver. Physics Review, 30, 201–214.

King, E.A. (1982) Refractory residues, condensates and chondrules from solar furnace epxeriments. Journal of Geophysical Research, 87, A429–A434.

Knudsen, M. (1909) Die Molekularströmung der Gase durch Offnungen und die Effusion. Annalen der Physik, 28, 999–1016.

Kozul, J., Ulmer, G.C., and Hewins, R. (1986) Allende inclusions are oxidized! EOS, 67, 300.

Kushiro, I., and Mysen, B.O. (1987) Experimental studies of the system Mg$_2$SiO$_4$-SiO$_2$-H$_2$ at pressures 10^{-2}–10^{-10} and at temperatures to 1650 °C: Application to condensation and vaporization processes in the primitive solar nebula. Earth and Planetary Science Letters (in press).

Larimer, J.W., and Anders, E. (1970) Chemical fractionation in meteorites—III. Major element fractionations in chondrites. Geochimica et Cosmochimica Acta, 34, 367–387.

Lattimer, M.J., and Grossman, L. (1978) Chemical condensation sequences in supernova ejecta. Moon and Planets, 19, 169–184.

Lin, D.N.C., and Papaloizou, J. (1980) On the structure and evolution of the primordial solar nebula. Nottingham Royal Astronomical Society, 191, 37–48.

Lou, V.K.L., Mitchell, T.E., and Heuer, A.H. (1985) Graphical displays of the thermodynamics of high-temperature gas-solid reactions and their application to oxidation of metals and evaporation of oxides. American Ceramic Society Journal, 68, 49–58.

Luth, R.W., and Boettcher, A.L. (1986) Hydrogen and the melting of silicates. American Mineralogist, 71, 264–276.

Luth, R.W., Mysen, B.O., and Virgo, D. (1987) A Raman spectroscopic study of the solubility behavior of H$_2$ in the system Na$_2$O-Al$_2$O$_3$-SiO$_2$-H$_2$O. American Mineralogist, 72, 481–486.

MacPherson, G.J., and Grossman, L. (1979) Melted and non-melted coarse-grained Ca-Al-rich inclusions in Allende. Meteoritics, 14, 479–480.

Mason, B. (1976) Data geochemistry: chap. B. Cosmochemistry. U.S. Geological Survey Professional Paper 440-B-1.

Masuda, A., and Tanaka, T. (1979) Experimental studies on behaviors of major and minor lithophile elements in vaporization under evacuated conditions. Meteoritics, 14, 13–28.

Motzfeldt, K. (1955) The thermal decomposition of sodium carbonate by the effusion method. Journal of Physical Chemistry, 59, 139–147.

Mysen, B.O., Virgo, D., and Kushiro, I. (1985) Experimental studies of condensation processes in silicate materials at low pressures and high temperatures. I. Phase equilibria in the system CaMgSi$_2$O$_6$-H$_2$ in the temperature range 1200–1500 °C and the pressure range (P_{H_2}) 10^{-6} to 10^{-9} bar. Earth and Planetary Science Letters, 75, 139–145.

Nagahara, H. (1981) Evidence for secondary origin of chondrules. Nature, 292, 135–136.

———(1984) Matrices of type-3 ordinary chondrites—Primitive nebular records. Geochimica et Cosmochimica Acta, 48, 2581–2596.

Niederer, F.R., and Papanastassiou, D.A. (1984) Ca isotopes in refractory inclusions. Geochimica et Cosmochimica Acta, 48, 1279–1294.

Onuma, N., Nishida, N., Ohtsuka, Y., Kinura, M., and Yanari, K. (1979) Origin and evolution of chondrules based on Na/Al dispersion and convergence in Yamoto-74 ordinary chondrites. Proceedings, 4th Symposium on Antarctic Meteorites, 206–215.

Palme, H., and Nickel, K.G. (1985) Ca/Al ratio and composition of the Earth's upper mantle. Geochimica et Cosmochimica Acta, 49, 2123–2132.

Paque, J. M., and Stolper, E. (1982) Experimental evidence for slow cooling of type B CAI's from a partially molten state (abs.). Lunar and Planetary Science, Proceedings, 4, 596–597.

Paule, R.C., and Margrave, J.L. (1967) Free-evaporation and effusion techniques. In J.L. Margrave, Ed., The characterization of high-temperature vapors, p. 130–151. Wiley, New York.

Porter, R.F., Chupka, W.A., and Inghram, M.G. (1955) Mass spectrometric study of gaseous species in the Si-SiO$_2$ system. Journal of Physical Chemistry, 23, 216–217.

Richet, P., and Bottinga, Y. (1986) Thermochemical properties of silicate glasses and liquids: A review. Reviews of Geophysics and Space Physics, 24, 1–26.

Robie, R.A., Hemingway, B.S., and Fisher, J.R. (1978) Thermodynamic properties of minerals and related substances at 298.15 K and 1 bar (10^5 pascals) pressure and at higher temperatures. U.S. Geological Survey Bulletin 1452.

Sata, T., Sasamata, H., Lee, L., and Maeda, E. (1978) Vaporization processes from magnesian minerals. Revue Hautes Refractories France, 15, 237–248.

Saxena, S.K., and Eriksson, G. (1983) High temperature phase equilibria in a solar-composition gas. Geochimica et Cosmochimica Acta, 47, 1865–1874.

Sosman, R.B. (1965) The phases of silica, 388 p. Rutgers University Press, New Brunswick, New Jersey.

Stolper, E. (1982) Crystallization sequences of Ca-Al-rich inclusions from Allende: An experimental study. Geochimica et Cosmochimica Acta, 46, 2159–2180.

Stull, D.R., and Prophet, H. (1971) JANAF thermochemical tables. U.S. National Bureau of Standards.

Tsuchiyama, A., Nagahara, H., and Kushiro, I. (1981) Vaporization of sodium from silicate melt spheres and its application to the formation of chondrules. Geochimica et Cosmochimica Acta, 45, 1357–1367.

Turekian, K.K., and Clark, S.P. (1969) Inhomogeneous accumulation of the earth from the primitive solar nebula. Earth and Planetary Science Letters, 6, 346–348.

Urey, H.C. (1961) Criticism of Dr. Mason's paper on "The origin of meteorites." Journal of Geophysical Research, 66, 1988–1991.

Van Schmus, W.R., and Wood, J.A. (1967) A chemical-petrologic classification for the chondritic meteorites. Geochimica et Cosmochimica Acta, 31, 747–765.

Wasson, J.T. (1972) Formation of ordinary chondrites. Reviews of Geophysics and Space Science, 10, 711–759.

———(1974) Meteorites, 316 p. Springer-Verlag, New York.

Weidenschilling, S.J. (1976) Accretion of the terrestrial planets: II. Icarus, 27, 161–170.

Wood, J.A. (1963) The origin of chondrules and chondrites. Icarus, 2, 152–180.

———(1967) Olivine and pyroxene composition in Type II carbonaceous chondrites. Geochimica et Cosmochimica Acta, 31, 2095–2108.

———(1981) The interstellar dust as a precursor of Ca, Al-rich inclusions in carbonaceous chondrites. Earth and Planetary Science Letters, 56, 32–44.

———(1984) On the formation of meteoritic chondrules by aerodynamic drag heating in the solar nebula. Earth and Planetary Science Letters, 70, 11–26.

Yoder, H.S. (1976) Generation of basaltic magma. National Academy of Sciences, Washington, D.C.